

Charles University in Prague
Faculty of Mathematics and Physics

MASTER THESIS



Štěpán Timr

Simulation of Processes in Cellular Membranes

Department of Chemical Physics and Optics

Supervisor of the master thesis: Pavel Jungwirth

Study programme: Physics

Specialization: Biophysics and Chemical Physics

Prague 2013

Acknowledgment

I would like to express my sincere gratitude to my supervisor Prof. Pavel Jungwirth for his perfect guidance, continuous support, and encouragement during my work on this thesis. I am no less indebted to Dr. Josef Lazar from the Institute of Nanobiology and Structural Biology GCRC AS CR for his help with polarization microscopy experiments and for supervising my work during three great summer projects, which gave inspiration and motivation to this thesis. I also thank the organizers of the Schola Ludus summer schools in Nové Hradky, of which the summer projects were part. Besides, I would like to thank the current and former members of the computational chemistry group of Prof. Pavel Jungwirth for a great team environment, especially Dr. Lukasz Cwiklik and Dr. Mario Vazdar, who introduced me to molecular dynamics simulations and advised me on one-photon transition dipole moment calculations, and Dr. Jiří Brabec, with whom I discussed calculations of two-photon absorption. In addition, my sincere thanks go to Prof. Martin Hof for providing me with the opportunity to prepare giant unilamellar vesicles in the laboratory of his research group at J. Heyrovský Institute of Physical Chemistry AS CR and to Dr. Martin Štefl for his repeated assistance with giant unilamellar vesicle preparation and performing preliminary measurements on them.

I declare that I carried out this master thesis independently and only with the cited sources, literature, and other professional sources.

I understand that my work relates to the rights and obligations under the Act No. 121/2000 Coll., the Copyright Act, as amended, in particular the fact that the Charles University in Prague has the right to conclude a license agreement on the use of this work as a school work pursuant to Section 60 paragraph 1 of the Copyright Act.

Prague, April 12, 2013

signature of the author

Název práce: Simulace procesů v buněčných membránách

Autor: Štěpán Timr

Katedra: Katedra chemické fyziky a optiky

Vedoucí diplomové práce: prof. Mgr. Pavel Jungwirth, CSc., DSc., Ústav organické chemie a biochemie Akademie věd České republiky

Abstrakt: Zkoumáním orientace fluorescenčních molekul ukotvených v buněčných membránách lze získat významné informace o struktuře membrán a procesech probíhajících v živých buňkách. V této diplomové práci nejprve popisujeme měření jedno- a dvoufotonového lineárního dichroismu fluorescenční sondy ve fosfolipidové membráně s přesně definovaným složením. Na základě experimentálních dat určujeme distribuci úhlu mezi dipólovým momentem jednofotonového přechodu a normálou membrány. Zároveň provádíme molekulární dynamiku fluorescenční sondy a kvantové výpočty jejích jedno- a dvoufotonových absorpčních vlastností. Srovnáním distribuce úhlů získané z experimentů s rozdělením předpovězeným simulacemi ověříme možnost určování orientace fluorescenční molekuly v lipidové membráně pomocí měření lineárního dichroismu. Rovněž prověříme možnost použití molekulárních simulací jako základu pro interpretaci experimentálních dat.

Klíčová slova: Orientace fluorescenčních sond, lineární dichroismus, dipólový moment přechodu, molekulární dynamika.

Title: Simulation of Processes in Cellular Membranes

Author: Štěpán Timr

Department: Department of Chemical Physics and Optics

Supervisor: prof. Mgr. Pavel Jungwirth, CSc., DSc., Institute of Organic Chemistry and Biochemistry, Academy of Sciences of the Czech Republic

Abstract: Probing orientations of fluorescent molecules embedded in or attached to cell membranes has a great potential to reveal information on membrane structure and processes occurring in living cells. In this thesis, we first describe one- and two-photon linear dichroism measurements on a fluorescent probe embedded in a phospholipid membrane with a well-defined lipid composition. On the basis of experimental data, we determine the distribution of the angle between the one-photon transition dipole moment of the probe and the membrane normal. At the same time, we perform molecular dynamics simulations of the fluorescent probe and quantum calculations of its one-photon and two-photon absorption properties. By comparing the orientational distribution gained from experiments with that predicted by simulations, we test the ability of linear dichroism measurements to report on the orientation of a fluorescent molecule in a lipid membrane. We also examine the applicability of molecular simulations as a basis for the interpretation of experimental data.

Keywords: Orientation of fluorescent probes, linear dichroism, transition dipole moment, molecular dynamics.

Contents

Introduction	3
1 Linear Dichroism and Its Measurements in Giant Unilamellar Vesicles	6
1.1 One-Photon and Two-Photon Absorption	6
1.2 Linear Dichroism vs Fluorescence Anisotropy	8
1.3 System of Interest	9
1.4 Experimental Methods and Image Analysis	11
1.5 Mathematical Interpretation of Experimental Data	14
1.6 Results	18
2 Molecular Dynamics	22
2.1 Classical Molecular Dynamics	22
2.2 Molecular Dynamics of Fluorescent Probes	26
2.3 Probe Parametrization and Simulation Protocol	29
2.4 Trajectory analysis	33
3 One-Photon Absorption	41
3.1 Molecule in an Electromagnetic Field	41
3.2 One-Photon Absorption Cross Section	43
3.3 Linear Response and Time-Dependent Density Functional Theory	45
3.4 One-Photon Transition Dipole Moment of F2N12S	48
4 Two-Photon Absorption	51
4.1 Two-Photon Absorption Cross Section	51
4.2 Approximation of a Two-Photon Transition Tensor by a One-Photon Transition Dipole Moment	52
4.3 Two-Photon Absorption of F2N12S	54
5 Orientational Distribution	57
5.1 Simulations vs Experiments	57
5.2 Convergence of Orientational Distributions Obtained from Simu- lations	61
Conclusion	64
Bibliography	66
List of Tables	77

Introduction

Biological membranes are essential constituents of every living cell. On one hand, the cell membrane separates cell's interior from the outer environment and thus plays a crucial role in maintaining stable conditions in cell's cytoplasm. While it keeps some substances out of the cell, it is permeable for others by means of passive or active transport. On the other hand, receptors bound to the cell membrane provide a vital connection to the outer world and enable the cell to respond to changes in the outer environment and to signals from other cells. Internal membranes, found especially in eukaryotic cells, divide cell's interior into various compartments or organelles and together with the cell membrane participate in many enzymatic processes (Alberts et al., 2002).

The basis for the current understanding of biological membranes is formed by the fluid mosaic model, first proposed by (Singer and Nicolson, 1972). This model describes a biological membrane as a lipid bilayer containing various protein molecules which float in the lipid environment and often extend to both leaflets of the bilayer. Lipids constituting the bilayer are amphiphilic molecules which consist of a polar, hydrophilic head group and typically two nonpolar, hydrophobic saturated or unsaturated fatty acid chains. The amphiphilic character of these lipids leads to spontaneous formation of bilayers, driven by an interplay between hydrophilic and hydrophobic interactions. Consequently, the polar head groups are exposed to the water environment, while the nonpolar fatty acid chains remain hidden in what is called the hydrophobic core of the bilayer. Not all lipids involved exhibit the same tendency to form bilayers, as the readiness of a particular lipid species to form bilayers largely depends on the temperature and on properties such as the size of the polar head group and the number, length, or saturation of the alkyl chains.

Lipid bilayers occurring in cells are typically composed of many different lipid species, which help fine-tune physical properties of the bilayer and are often necessary for a proper function of various membrane proteins. Head groups of membrane lipids can be neutral or negatively charged and possess different dipole moments. Charged head groups contribute to the surface potential of the bilayer, and the dipole moments of head groups, together with those of water and ester groups, create a dipole potential localized between the membrane surface and the hydrophobic core of the bilayer. A common feature of membrane lipid species in cells is their asymmetrical distribution between the two leaflets of the bilayer. Membrane lipids can be divided into three main categories: phospholipids, glycolipids, and steroids. Cholesterol, the most abundant member of the steroid group

in mammalian cells, significantly influences the fluidity and other properties of the bilayer.

Depending on the temperature and composition, lipid bilayers can exist in three different phase states: gel, liquid ordered, or liquid disordered. These phases primarily differ in the order of fatty acid chains and in microviscosity, i.e., the friction of the rotational and translational motion in the bilayer. While fatty acid chains are highly ordered and lateral diffusion is restricted in the former, the fluidity of the latter two is an essential property of all lipid bilayers found in cells. Liquid ordered phase is believed to exist in biological membranes in form of transient domains, called rafts, enriched with cholesterol and saturated lipids (Simons and Ikonen, 1997). However, the size and function of these domains are still being investigated (Lingwood and Simons, 2010).

To shed light on the complex structure and dynamics of lipid bilayers, a number of different techniques have been used by experimentalists. These techniques include X-ray crystallography, neutron scattering, nuclear magnetic resonance (NMR), electron paramagnetic resonance (EPR), electron microscopy, and atomic-force microscopy (AFM). A prominent place among these methods, however, have fluorescence techniques, largely due to their sensitivity and the ability to probe living biological samples. Since lipid molecules themselves are nonfluorescent, the use of fluorescence techniques requires addition of fluorescent probes into lipid bilayers. A number of environment-sensitive fluorescent probes have already been designed to study properties such as lipid order, microviscosity, polarity, hydration, environment relaxation, and static electric fields in bilayers (Demchenko et al., 2009). Common quantities detected using fluorescence techniques include steady-state or time-resolved fluorescence intensity, excitation and emission spectra, fluorescence quantum yield and lifetime, and fluorescence anisotropy (Lakowicz, 2006; Hof et al., 2005).

An important characteristic of fluorescent probes is their orientation relative to the bilayer normal. Not only is its knowledge useful for a rational development of new environment-sensitive probes, but it can itself provide valuable information on the structure and order of the bilayer environment. The orientation of fluorescent probes can be examined by measuring the above mentioned fluorescence anisotropy. Another technique, offering several significant advantages over fluorescence anisotropy measurements, consists in measuring linear dichroism, i.e., the anisotropy of polarized light absorption. The process of absorption by a fluorescent probe can involve a single photon, or it can be of a higher order, involving two or more photons. Linear dichroism measured upon two-photon absorption, for example, has been employed to observe the effect of cholesterol depletion on the orientation of fluorescent probes (Benninger et al., 2005) or to determine fat-

ty acid chain order in lipid bilayers with varying cholesterol content (Farkas and Webb, 2010). Moreover, the applications of linear dichroism measurements are not restricted to probing properties of lipid bilayers. As demonstrated in (Lazar et al., 2011) with a contribution of the author of this thesis, linear dichroism measurements can be used in living cells to image changes in conformation of fluorescent protein-tagged membrane proteins. This should open the way for a development of genetically encoded fluorescent probes of various processes occurring in living cells, such as changes in ion concentration or membrane voltage, and for gaining insight into membrane protein structure. Nevertheless, a key question is how much information on the actual distribution of orientations can be obtained from linear dichroism measurements. It turns out (Reeve et al., 2012) that unless a particular character of the orientational distribution is assumed (e.g., Gaussian), it is not possible to recover the distribution unambiguously from experiments.

Recent years have seen rapid progress in the field of computer simulations of lipid bilayers (Lyubartsev and Rabinovich, 2011). Molecular dynamics simulations of lipid bilayers have yielded atomistic details which could not previously be obtained from experiments. This suggests an idea to combine results of molecular dynamics simulations of a particular fluorescent probe with information on its absorption properties, obtained from quantum calculations, and thus establish a basis for interpretation of experimental data and verify general assumptions made regarding the orientational distribution.

In this thesis, as a proof of principle, we focus on the orientational distribution of a fluorescent probe 4'-N,N-diethylamino-6-(N-dodecyl-N-methyl-N-(3-sulfopropyl))ammoniomethyl-3-hydroxyflavone (F2N12S) bound in a phospholipid bilayer consisting of 1-palmitoyl-2-oleoylphosphatidylcholine (POPC). We report on a combination of one-photon and two-photon linear dichroism measurements conducted with synthetically prepared giant unilamellar vesicles (GUVs) and analyze the data in order to obtain experimental information on the orientational distribution. At the same time, we perform molecular dynamics simulations of an F2N12S probe in a POPC bilayer and quantum calculations of the probe's one-photon and two-photon absorption properties. By comparing experimental estimates of the orientational distribution with computational results, we test whether the assumptions made regarding the orientational distribution are supported by simulations. In addition, we discuss the accuracy and applicability of molecular dynamics simulations in modeling the orientational distribution of a fluorescent probe in a phospholipid membrane.

1. Linear Dichroism and Its Measurements in Giant Unilamellar Vesicles

In this chapter, we first briefly introduce the basic concepts of fluorescence and discuss advantages of linear dichroism measurements over fluorescence anisotropy. Next, we describe our system of interest and the experimental methods used for its preparation and investigation. We mention the procedure of image processing and construct a mathematical model of absorption anisotropy which we finally employ to interpret the experimental data obtained.

1.1 One-Photon and Two-Photon Absorption

Fluorescence is the emission of visible light by a molecule after absorption of visible or invisible electromagnetic radiation. When a molecule in a singlet ground electronic state S_0 absorbs electromagnetic radiation, it can be excited to a higher singlet electronic state S_n . At the same time, the excitation can change the vibrational state of the molecule. In most cases, the excitation proceeds from the lowest vibrational state, as it is the most populated one at room temperature. Regardless of the electronic or vibrational state they were excited to, most molecules in a condensed phase quickly end up in the lowest vibrational state of the first excited electronic state S_1 as a result of a process called internal conversion, which occurs within 10^{-12} s (Lakowicz, 2006). The lifetime of S_1 is typically of the order of 10^{-8} s (Lakowicz, 2006). Fluorescence is then a consequence of the transition from S_1 back to the ground state S_0 . Alternatively, molecules can undergo a conversion from S_1 to a triplet state T_1 , called intersystem crossing. The emission of light caused by the transition from T_1 to S_0 is called phosphorescence. It differs from fluorescence in the lifetime of T_1 , which is several orders of magnitude longer than that of S_1 . An illustration of energy levels and transitions between them is presented by a Jablonski diagram in Figure 1.1.

An ordinary process of absorption involves a single photon. This process is called one-photon (1P) absorption. However, when the intensity of radiation is sufficiently high, two or more photons can be absorbed at a time, also promoting the molecule from its ground electronic state to an excited state. In general, this process is referred to as multiphoton absorption. Out of these higher-order absorption processes, especially two-photon (2P) absorption has started to be

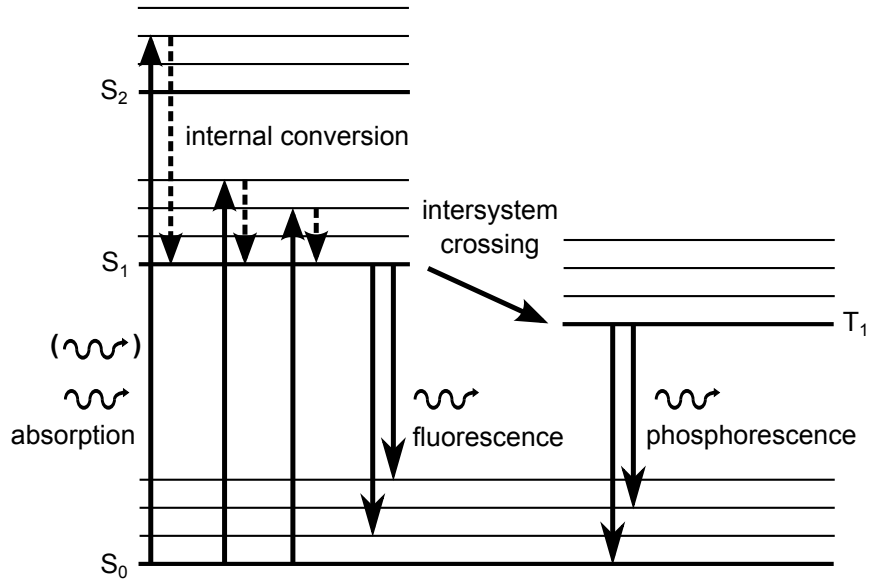


Figure 1.1: A Jablonski diagram.

widely used in fluorescence imaging.

In regular 1P absorption, the absorption rate $R^{(1)}$ depends linearly on the intensity I of the excitation radiation,

$$R^{(1)} = \sigma^{(1)} I. \quad (1.1)$$

Here, $\sigma^{(1)}$ is the cross section of 1P absorption, which is dependent on the frequency of the incoming radiation. Its exact shape is discussed in Chapter 3. In contrast, 2P absorption exhibits a quadratic dependence of the absorption rate $R^{(2)}$ on the intensity I of the excitation radiation,

$$R^{(2)} = \frac{1}{2} \sigma^{(2)} I^2. \quad (1.2)$$

A detailed treatment of the two-photon cross section $\sigma^{(2)}$ can be found in Chapter 4. The appearance of the factor $\frac{1}{2}$ in (1.2) is a matter of convention and reflects the fact that two photons are required to promote a single molecule to an excited state.

2P absorption offers some significant benefits over 1P absorption, which are especially useful for imaging of biological tissues even in living organisms (Piston, 1999; Svoboda and Yasuda, 2006). First, longer-wavelength radiation, typically from the far red or near IR region of the spectrum, is used to excite fluorescent probes rather than the short-wavelength visible light or near UV radiation predominantly employed in 1P absorption. The longer-wavelength radiation penetrates more easily through the tissue, up to 1 mm deep. Second, the quadratic dependence of 2P absorption rate on the intensity of excitation radiation in (1.2)

implies that molecules are only excited in a very small region around the focal point. This substantially reduces the distorting effects of background fluorescence from nonfocal areas and enables scanning the tissue with a 3D resolution. Last but not least, the significantly lower contribution of background fluorescence greatly simplifies the experimental setup, since there is no need of pinholes, which are used in 1P confocal microscopy and whose proper alignment tends to be difficult.

1.2 Linear Dichroism vs Fluorescence Anisotropy

The absorption probability of linearly polarized electromagnetic radiation depends on the orientation of its electric vector relative to the geometry of the molecule interacting with the electromagnetic field. In the case of 1P absorption, each transition between the ground state and an excited state of a molecule is assigned a vector called the one-photon absorption transition dipole moment (1P TDM). The absorption probability is maximal if the electric vector is aligned with the 1P TDM. On the other hand, if the two vectors are not parallel, the absorption probability decreases. The cross section of 1P absorption satisfies

$$\sigma^{(1)} \propto \cos^2 \beta, \quad (1.3)$$

where β denotes the angle between the 1P TDM and the electric vector \mathbf{e} of the excitation radiation. In the case of 2P absorption, each transition is assigned a tensor rather than a vector. However, for many molecules, satisfying conditions discussed in Chapter 4, the tensor only has a single dominant eigenvalue, and the anisotropy of absorption can be well described by the corresponding 1P TDM vector. In this case, the 2P cross section does not depend on the square but on the fourth power of $\cos \beta$,

$$\sigma^{(2)} \propto \cos^4 \beta, \quad (1.4)$$

since 2P absorption is a second-order process.

The dependence of absorption probability on molecular orientation relative to light polarization opens the door for probing orientational distributions of molecules in anisotropic systems, such as bilayers, using linearly polarized visible light, near UV, or near IR radiation. The anisotropy in absorption of radiation linearly polarized along two perpendicular directions is called linear dichroism (LD). Because fluorescence intensity is proportional to the absorption cross section, LD can be quantified by comparing intensities of fluorescence (denoted, e.g., by I_h and I_v) excited with two perpendicular polarizations. LD is sometimes expressed

as the difference between I_h and I_v (Benninger et al., 2005),

$$LD = I_h - I_v. \quad (1.5)$$

In this thesis, however, we adopt a different way of quantifying LD in terms of the dichroic ratio r , defined as (Lazar et al., 2011)

$$r = \frac{I_h}{I_v}, \quad (1.6)$$

since this quantity does not depend on the concentration of absorbing fluorescent probes in the examined region.

Another way of investigating molecular orientation consists in measuring fluorescence anisotropy (FA), i.e., the polarization of fluorescence after excitation with linearly polarized light. Light emitted by a molecule which is returning to its ground state is linearly polarized along a vector called the emission dipole moment. This vector is often not parallel to the 1P TDM, which diminishes observed FA. Furthermore, FA is decreased by rotational diffusion of fluorescent probes between the events of excitation and emission. Another cause of the decrease in FA can be energy transfer, pronounced at high concentrations of fluorescent probes. While the decay of FA between excitation and emission can be used, e.g., to determine rotational diffusion coefficients of fluorescent probes embedded in membranes and thus to measure membrane microviscosity (Lakowicz, 2006), the information on the steady-state orientational distribution of fluorescent probes in anisotropic environments is partially lost because of the depolarizing effects. Moreover, the polarization of fluorescence detected in FA measurements is influenced by scattering of emitted light within the sample. LD measurements are not affected by the above issues, which, compared to FA, makes them more convenient for determining orientational distributions of fluorescent probes in anisotropic systems. Concerning LD measurements, worthwhile mentioning is also the absence of polarization optical components in the emission pathway and the possibility of using high numerical aperture objective lenses, which improves the efficiency of fluorescence collection.

1.3 System of Interest

To test how much information on the orientational distribution of a fluorescent probe can be obtained from LD measurements and to compare the experimental results with simulations, we selected a model system comprising a POPC bilayer stained with the F2N12S probe. The structures of the two molecules are shown

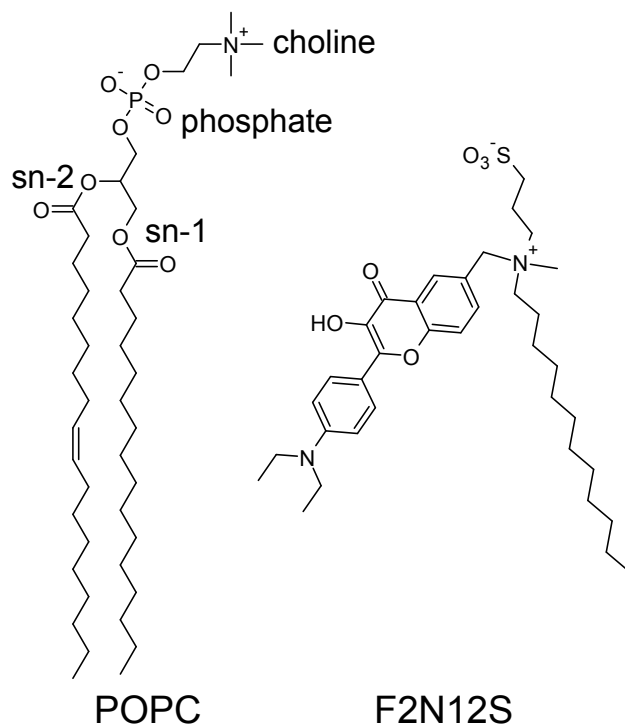


Figure 1.2: Structures of POPC and F2N12S.

in Figure 1.2.

POPC belongs to the class of phosphatidylcholines, which are major constituents of biological membranes (Alberts et al., 2002). POPC consists of a polar head group formed by glycerol, phosphate, and choline, and two hydrophobic fatty acid chains, one of which is unsaturated.

F2N12S is a 3-hydroxyflavone based fluorescent probe which was designed for detection of apoptosis, i.e., the process of programmed cell death (Shynkar et al., 2007). Furthermore, it has been used to examine the presence of liquid ordered phase in cell membranes (Oncul et al., 2010). In its excited state, the probe may undergo an excited-state intramolecular proton transfer reaction, resulting in a presence of two bands in its emission spectrum (Das et al., 2008). The positions of these bands and their relative intensities are sensitive to the polarity and hydration of the environment. The probe can be excited using 1P as well as 2P absorption (Klymchenko et al., 2009).

In experiments, the POPC bilayer was realized in form of giant unilamellar vesicles (GUVs). F2N12S probe was added to POPC before GUV preparation. The procedure of GUV preparation is described in the following section.

1.4 Experimental Methods and Image Analysis

Vesicles are spherical structures formed by one or more lipid bilayers. While multilamellar vesicles comprise several bilayers, unilamellar vesicles only consist of a single bilayer. On the basis of their size, unilamellar vesicles can be divided into three main categories (Stöckl and Herrmann, 2010): (1) small unilamellar vesicles (SUVs) have a diameter of several nanometers, (2) large unilamellar vesicles (LUVs) with a typical diameter between 100–200 nm, (3) giant unilamellar vesicles (GUVs) with a diameter up to several tens of micrometers. The size of GUVs makes them suitable for visualization by fluorescence microscopy and allows their use as models of cell membranes.

In general, GUVs are prepared by the hydration of a dried lipid film (Rodriguez et al., 2005). There are two techniques used for GUV formation: gentle hydration (Reeves and Dowben, 1969; Darszon et al., 1980; Needham et al., 1988) and electroformation (Angelova and Dimitrov, 1986; Mathivet et al., 1996). While the former relies solely on spontaneous GUV formation from the lipid film after its hydration by an aqueous solution with a fine-tuned osmotic pressure and ionic strength, the latter adds AC field to facilitate the process of vesicle formation. The AC field is believed to promote vesicle formation by inducing mechanical vibrations of the lipid structures (Mathivet et al., 1996). There are several advantages of electroformation over gentle hydration (Morales-Pennington et al., 2010). Electroformation offers a higher yield and produces GUVs with fewer defects and a lower ratio of unwanted multilamellar vesicles. Moreover, it does not require the presence of a fraction of negatively charged lipids in the mixture. On the other hand, its use with charged lipids is limited.

Our GUVs were produced using an electroformation protocol described in (Stöckl et al., 2010). First, a mixture containing 97 mol % of POPC, 2 mol % of biotinylated DPPE, and 1 mol % of the F2N12S probe with a total lipid concentration equal to 200 nmol in 100 μ l of chloroform was prepared in a small glass test tube. Next, the lipid mixture was spread on two titanium plate electrodes, which were preheated to 48 °C. The electrodes were placed into a dessicator and kept under the vacuum for two hours. Subsequently, the pair of electrodes was isolated using Parafilm, and the swelling chamber was filled with 0.1 M sucrose solution ($\Pi = 103$ mOsm). Sinusoidal voltage was applied to the electrodes in three stages: During the initiation stage, which took 50 minutes, voltage amplitude was linearly increased in 50 mV intervals from 150 mV to 1.1 V, and frequency was 10 Hz. During the GUV formation stage with a duration of 90 minutes, voltage amplitude was held at 1.1 V and frequency at 10 Hz. Finally, the stage of GUV detaching lasted for 30 minutes, with a voltage amplitude of 1.3 V and a fre-

quency of 4 Hz. The temperature of the titanium electrodes was kept at 48 °C during the whole electroformation process. Newly formed GUVs were carefully transferred to an Eppendorf test tube, stored at room temperature and used within 2–3 days. Prior to measurements, GUVs were diluted 20 times in a glucose solution (60 mM glucose, 10 mM NaCl, 10 mM HEPES, $\Pi = 103$ mOsm) and pipetted (400 μ l) into an imaging chamber (μ -Slide 8 well, iBidi, Germany) which was coated with a layer of biotinylated albumin to which streptavidin was bound. The strong interaction between streptavidin and biotinylated DPPE contained in GUV membranes was used to immobilize GUVs for measurements.

Polarization microscopy experiments were performed on a custom-built confocal laser scanning microscope based on the iMic2 microscope (Till Photonics, Germany) at a temperature of 20 °C. Imaging was carried out using a UApoPlan/IR $\times 60$ NA1.2 water-immersion objective lens (Olympus, Japan).

The 1P setup is shown in Figure 1.3. The fluorescent probe was excited by a 405 nm laser (50 mW, PowerLaser, Czech Republic). The beam diameter was restricted by a pinhole to ~ 0.5 mm, so that the light emerging from the objective formed a narrow ($\sim 20^\circ$) cone. A 500 nm short-pass dichroic mirror was placed outside the scanner to separate fluorescence from excitation light. Fluorescence was directed through a confocal pinhole (LSM410, Carl Zeiss, Germany) to a photomultiplier (R6357, Hamamatsu Photonics, Japan) equipped with a Brightline 542/27 emission filter (Semrock, USA). Polarization of the excitation beam was alternated between horizontal and vertical direction by a polarization modulator (RPM-2P, Innovative Bioimaging, USA) operated at 100 kHz, in synchrony with acquisition of individual pixels by the microscope.

The 2P setup is depicted in Figure 1.4. The Chameleon Ultra II laser (Coherent, Inc., USA) with group-velocity-dispersion compensation was tuned at 810 nm, and a 735 nm long-pass dichroic mirror (Semrock, USA) was used to separate fluorescence from excitation light. The photomultiplier was equipped with a HQ700SP-2P emission filter (Chroma, USA). In contrast to the 1P setup, no confocal pinhole was necessary, as 2P absorption guaranteed localization of excitation in a small volume around the focal point, and as a consequence, the fluorescence signal contained little background noise.

Regardless of whether the images of GUVs were acquired using 1P or 2P excitations, the following procedure was used for their processing. The background present in the images was subtracted using a mean value obtained in regions that did not contain any GUVs. A correction factor compensating for potentially different intensities of the two perpendicular polarizations of the excitation beam was established from the fluorescence signal of an isotropic sample. GUV membranes were marked with splines obtained using the Active Cells plug-

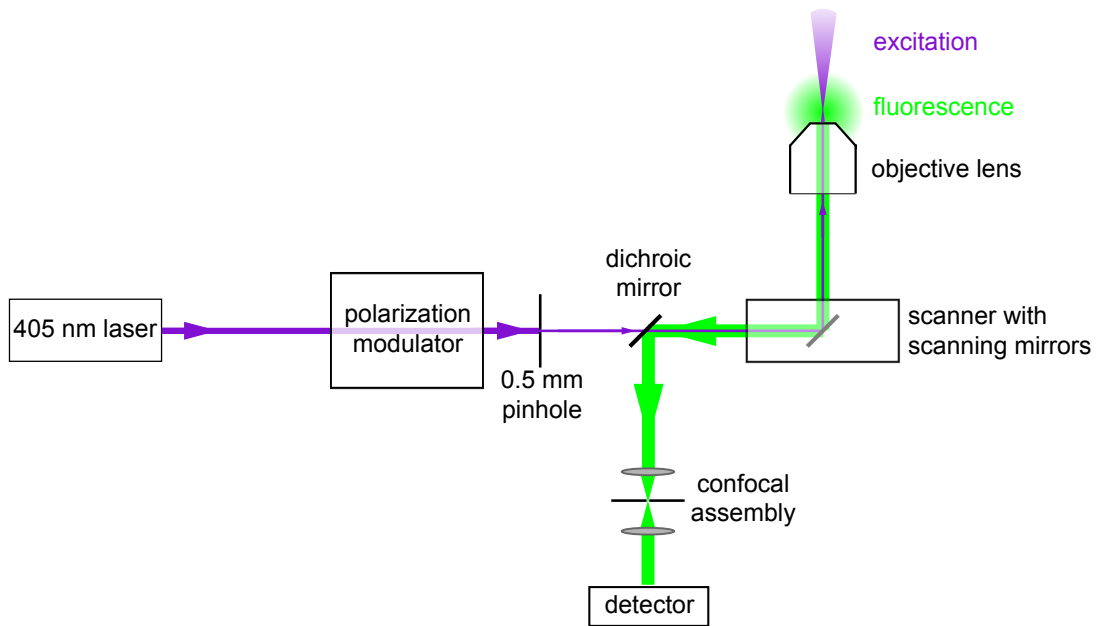


Figure 1.3: 1P experimental setup.

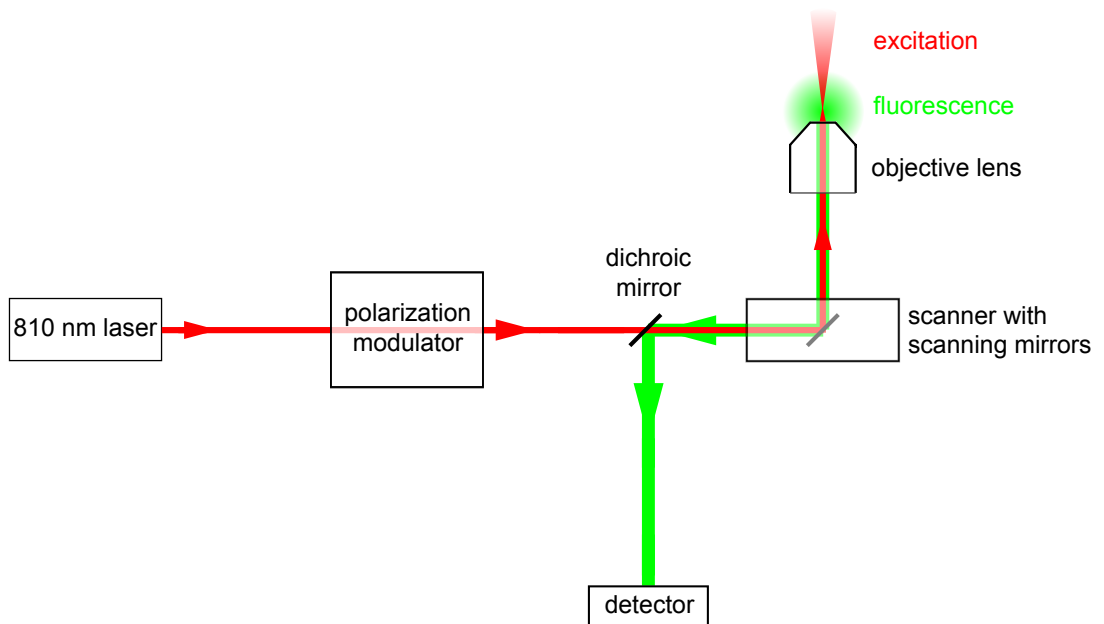


Figure 1.4: 2P experimental setup.

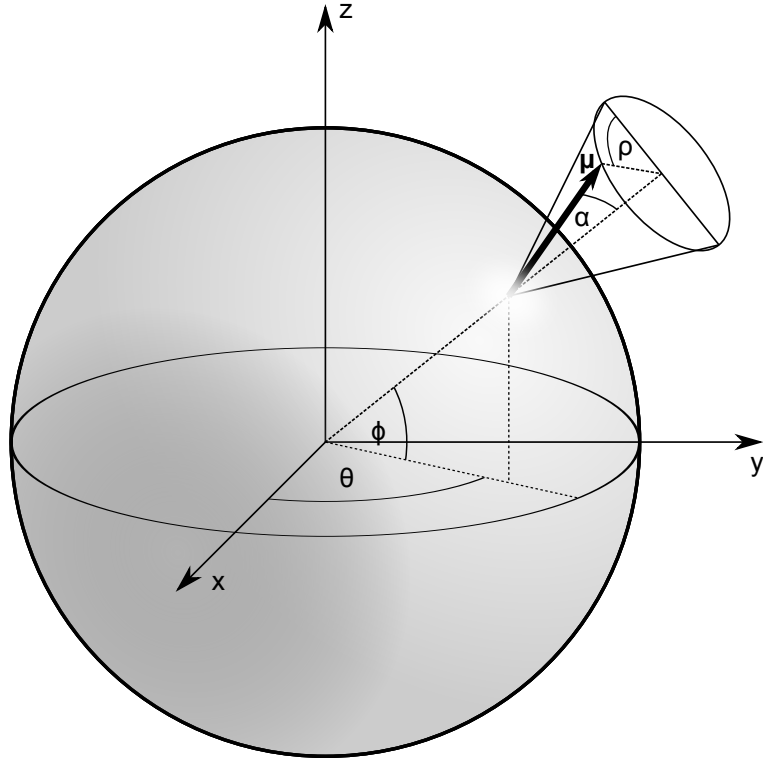


Figure 1.5: Geometrical model of the 1P TDM orientation of a fluorescent probe embedded in a membrane.

in (Delgado-Gonzalo et al., 2012a,b) available in the image analysis software Icy (de Chaumont et al., 2012). For each polarization, the intensities of pixels located within a distance of five pixels from the spline were binned according to the angle of the spline normal relative to the horizontal direction. For each of these 3° bins, the value of the dichroic ratio r was calculated. We quantitatively analyzed at least ten representative GUVs, both for 1P and 2P imaging experiments.

1.5 Mathematical Interpretation of Experimental Data

Experimental data processing yields the dependence of the dichroic ratio r on the direction of the bilayer normal. In order to extract quantitative information on the orientational distribution of a fluorescent probe embedded in the bilayer from this dependence, we employ a mathematical model introduced in this section.

The mathematical model describes fluorescent probe orientation in terms of two angles: the tilt angle α of the 1P TDM with respect to the bilayer normal and the angle ρ , corresponding to the rotation of the 1P TDM around the bilayer normal. The direction of the bilayer normal relative to a reference coordinate system is expressed in terms of two angles θ and ϕ . The definition of the angular

parameters is illustrated in Figure 1.5.

We denote the 1P TDM by $\boldsymbol{\mu}$ and assume for the purpose of geometric considerations that it is of unit length. Then the 1P TDM can be expressed in the reference coordinate system as

$$\boldsymbol{\mu}(\alpha, \rho, \theta, \phi) = \mathbf{R}_3(\theta) \mathbf{R}_2(-\phi) \mathbf{R}_1(\rho) \mathbf{R}_2(-\alpha) \begin{pmatrix} 1 \\ 0 \\ 0 \end{pmatrix}, \quad (1.7)$$

where $\mathbf{R}_1(\tau)$, $\mathbf{R}_2(\tau)$, and $\mathbf{R}_3(\tau)$ are rotation matrices defined as

$$\begin{aligned} \mathbf{R}_1(\tau) &= \begin{pmatrix} 1 & 0 & 0 \\ 0 & \cos \tau & -\sin \tau \\ 0 & \sin \tau & \cos \tau \end{pmatrix}, & \mathbf{R}_2(\tau) &= \begin{pmatrix} \cos \tau & 0 & \sin \tau \\ 0 & 1 & 0 \\ -\sin \tau & 0 & \cos \tau \end{pmatrix}, \\ \text{and } \mathbf{R}_3(\tau) &= \begin{pmatrix} \cos \tau & -\sin \tau & 0 \\ \sin \tau & \cos \tau & 0 \\ 0 & 0 & 1 \end{pmatrix}. \end{aligned} \quad (1.8)$$

The 1P TDM, of course, is not expected to assume only a single value of α . Instead, we expect a distribution $F(\alpha)$ of the tilts relative to the bilayer normal. At the same time, rotation around the membrane normal can be regarded as isotropic, and thus, we can simply integrate over ρ . Given that the electric vector of the excitation radiation points in the direction expressed by a unit vector \mathbf{e} , the expected fluorescence intensity in the case of 1P absorption can be written as

$$I_{\mathbf{e}}^{(1P)}(\theta, \phi) = \frac{I_0}{2\pi} \int_0^{2\pi} d\rho \int_0^{\pi/2} d\alpha F(\alpha) (\boldsymbol{\mu}(\alpha, \rho, \theta, \phi) \cdot \mathbf{e})^2, \quad (1.9)$$

in accord with (1.3). In the case of 2P absorption, using (1.4), we analogously obtain

$$I_{\mathbf{e}}^{(2P)}(\theta, \phi) = \frac{I'_0}{2\pi} \int_0^{2\pi} d\rho \int_0^{\pi/2} d\alpha F(\alpha) (\boldsymbol{\mu}(\alpha, \rho, \theta, \phi) \cdot \mathbf{e})^4. \quad (1.10)$$

Since we imaged GUVs with the focal plane of the objective set close to the GUV equatorial plane, we can consider ϕ to be equal to zero. This will significantly simplify our further formulas.

Let us now orient the reference coordinate system in such a way that the z axis points in the direction of the excitation laser beam, while the x and y axes are aligned with the two linear polarizations used for LD measurements. The x axis is identified with the polarization that appears horizontal in GUV images and the y axis with that appearing vertical. Furthermore, let $\langle g(\alpha) \rangle$ represent the

mean value of a function $g(\alpha)$,

$$\langle g(\alpha) \rangle = \int_0^{\pi/2} d\alpha F(\alpha) g(\alpha). \quad (1.11)$$

Evaluating (1.9), we obtain formulas for the intensities of fluorescence excited with horizontally and vertically polarized light in the case of 1P absorption:

$$I_h^{(1P)}(\theta) = I_0 \left(\langle \cos^2 \alpha \rangle \cos^2 \theta + \frac{1}{2} \langle \sin^2 \alpha \rangle \sin^2 \theta \right), \quad (1.12)$$

$$I_v^{(1P)}(\theta) = I_0 \left(\langle \cos^2 \alpha \rangle \sin^2 \theta + \frac{1}{2} \langle \sin^2 \alpha \rangle \cos^2 \theta \right). \quad (1.13)$$

Similarly, for 2P absorption we obtain from (1.10):

$$I_h^{(2P)}(\theta) = I_0' \left(\langle \cos^4 \alpha \rangle \cos^4 \theta + \frac{3}{16} \langle \sin^2 2\alpha \rangle \sin^2 2\theta + \frac{3}{8} \langle \sin^4 \alpha \rangle \sin^4 \theta \right), \quad (1.14)$$

$$I_v^{(2P)}(\theta) = I_0' \left(\langle \cos^4 \alpha \rangle \sin^4 \theta + \frac{3}{16} \langle \sin^2 2\alpha \rangle \sin^2 2\theta + \frac{3}{8} \langle \sin^4 \alpha \rangle \cos^4 \theta \right). \quad (1.15)$$

The ratio of (1.12) and (1.13) and the ratio of (1.14) and (1.15) provide us with a prediction of the dichroic ratio r for 1P and 2P absorption, respectively, given the bilayer normal is oriented at an angle θ relative to the horizontal polarization.

A closer look at (1.12)–(1.15) reveals that there are only two independent parameters determining how the 1P or 2P dichroic ratio r depends on θ , namely, $\langle \cos^2 \alpha \rangle$ and $\langle \cos^4 \alpha \rangle$. The remaining mean values in (1.12)–(1.15) can be written as a combination of these two parameters. Therefore, $\langle \cos^2 \alpha \rangle$ and $\langle \cos^4 \alpha \rangle$ present the actual information on the distribution function $F(\alpha)$ that can be obtained from a combination of 1P and 2P LD measurements.

The knowledge of as few as two parameters, gained by fitting 1P and 2P experimental dependencies of r on θ with theoretical predictions based on (1.12)–(1.15), is clearly not sufficient to reconstruct a general distribution function from experiments. However, if a particular character of the distribution function is assumed, two parameters may be enough to obtain an unambiguous result. The distribution function $F(\alpha)$ can be written as

$$F(\alpha) = \sin \alpha f(\alpha), \quad (1.16)$$

where the $\sin \alpha$ term reflects the changing density of states with changing α , and $f(\alpha)$ is a function satisfying a normalization condition

$$1 = \int_0^{\pi/2} d\alpha \sin \alpha f(\alpha). \quad (1.17)$$

The first approximation to the actual $f(\alpha)$ is a Gaussian function with a peak at α_0 and a width determined by σ ,

$$f(\alpha) \approx f_{\text{Gauss}}(\alpha) = A \exp\left(-\frac{(\alpha - \alpha_0)^2}{2\sigma^2}\right), \quad (1.18)$$

where A is a normalization factor. Another approximation of $f(\alpha)$ relies on a truncated expansion of $f(\alpha)$ in the basis of Legendre polynomials. The function $f(\alpha)$ can be expanded on $(0, \pi)$ as (Castanho et al., 2003; Fraňová et al., 2010)

$$f(\alpha) = \sum_{L=0}^{\infty} \frac{1}{2} (2L+1) \langle P_L \rangle P_L(\cos \alpha), \quad (1.19)$$

where

$$\langle P_L \rangle = \int_0^{\pi} d\alpha \sin \alpha f(\alpha) P_L(\cos \alpha). \quad (1.20)$$

Legendre polynomials are defined as (Reed and Simon, 1979)

$$P_L(x) = \frac{1}{L!} \left(\frac{d}{dt} \right)^L (1 - 2xt + t^2)^{-1/2} \Big|_{t=0} \quad (1.21)$$

and satisfy for all nonnegative integers L and M (Reed and Simon, 1979)

$$\int_{-1}^1 dx P_L(x) P_M(x) = \frac{2}{2L+1} \delta_{LM}. \quad (1.22)$$

Since it is not possible to distinguish between α and $\pi - \alpha$ on the basis of optical experiments, we require that $f(\alpha) = f(\pi - \alpha)$ for all α in $(0, \pi)$. Therefore, all terms with an odd L vanish from (1.19), and we can restrict ourselves again to $(0, \pi/2)$. After replacing the interval of integration in (1.20) by $(0, \pi/2)$, i.e.,

$$\langle P_L \rangle = \int_0^{\pi/2} d\alpha \sin \alpha f(\alpha) P_L(\cos \alpha), \quad (1.23)$$

(1.19) becomes

$$f(\alpha) = \sum_{L=0; L \text{ even}}^{\infty} (2L+1) \langle P_L \rangle P_L(\cos \alpha). \quad (1.24)$$

The first term in (1.24) is trivial, since $P_0(\cos \alpha)$ is identically equal to 1, and $\langle P_L \rangle = 1$ because of the normalization condition (1.17). The second and the third term can be obtained from 1P and 2P LD measurements, as $\langle P_2 \rangle$ and $\langle P_4 \rangle$ can

be expressed using $\langle \cos^2 \alpha \rangle$ and $\langle \cos^4 \alpha \rangle$,

$$\langle P_2 \rangle = \frac{1}{2} (3\langle \cos^2 \alpha \rangle - 1), \quad (1.25)$$

$$\langle P_4 \rangle = \frac{1}{8} (35\langle \cos^4 \alpha \rangle - 30\langle \cos^2 \alpha \rangle + 3). \quad (1.26)$$

Therefore, the combination of 1P and 2P LD experiments yields an estimate of the actual $f(\alpha)$ relying on the first three terms of the Legendre expansion (1.24),

$$f(\alpha) \approx f_{\text{Leg}}(\alpha) = 1 + 5 \langle P_2 \rangle P_2(\cos \alpha) + 9 \langle P_4 \rangle P_4(\cos \alpha). \quad (1.27)$$

The approximation $f_{\text{Leg}}(\alpha)$, based on the truncated Legendre expansion, may not be sufficiently close to the actual $f(\alpha)$. In addition, $f_{\text{Leg}}(\alpha)$ often assumes negative values, which is certainly not desirable, since the distribution function $F(\alpha)$ must be nonnegative. Therefore, an alternative way for obtaining an approximation of $f(\alpha)$ has been proposed (Castanho et al., 2003). Its idea is to search for a normalized function $f_S(\alpha)$ which maximizes the entropy functional,

$$S(f_S(\alpha)) = \int_0^{\pi/2} d\alpha \sin \alpha f_S(\alpha) \ln f_S(\alpha), \quad (1.28)$$

and, at the same time, satisfies the following constraints:

$$\langle P_2 \rangle = \int_0^{\pi/2} d\alpha \sin \alpha f_S(\alpha) P_2(\cos \alpha), \quad (1.29)$$

$$\langle P_4 \rangle = \int_0^{\pi/2} d\alpha \sin \alpha f_S(\alpha) P_4(\cos \alpha). \quad (1.30)$$

The problem can be solved by using the technique of Lagrange multipliers with a result

$$f_S(\alpha) = \frac{\exp(\lambda_2 P_2(\cos \alpha) + \lambda_4 P_4(\cos \alpha))}{\int_0^{\pi/2} d\alpha \sin \alpha \exp(\lambda_2 P_2(\cos \alpha) + \lambda_4 P_4(\cos \alpha))}. \quad (1.31)$$

Here, λ_2 and λ_4 are Lagrange multipliers assigned to $\langle P_2 \rangle$ and $\langle P_4 \rangle$, respectively. They are calculated by substituting (1.31) into (1.29) and (1.30) and solving the resulting system of two nonlinear equations.

1.6 Results

We recorded fluorescence from 11 GUVs using 1P absorption and from 10 GUVs using 2P absorption. In both sets of GUVs, we found weak but clearly observable linear dichroism. In the case of 1P absorption, the maximum of $\log_2 r$ was close to 0.25 (i.e., $r = 1.19$), while in the case of 2P absorption, the maximum value

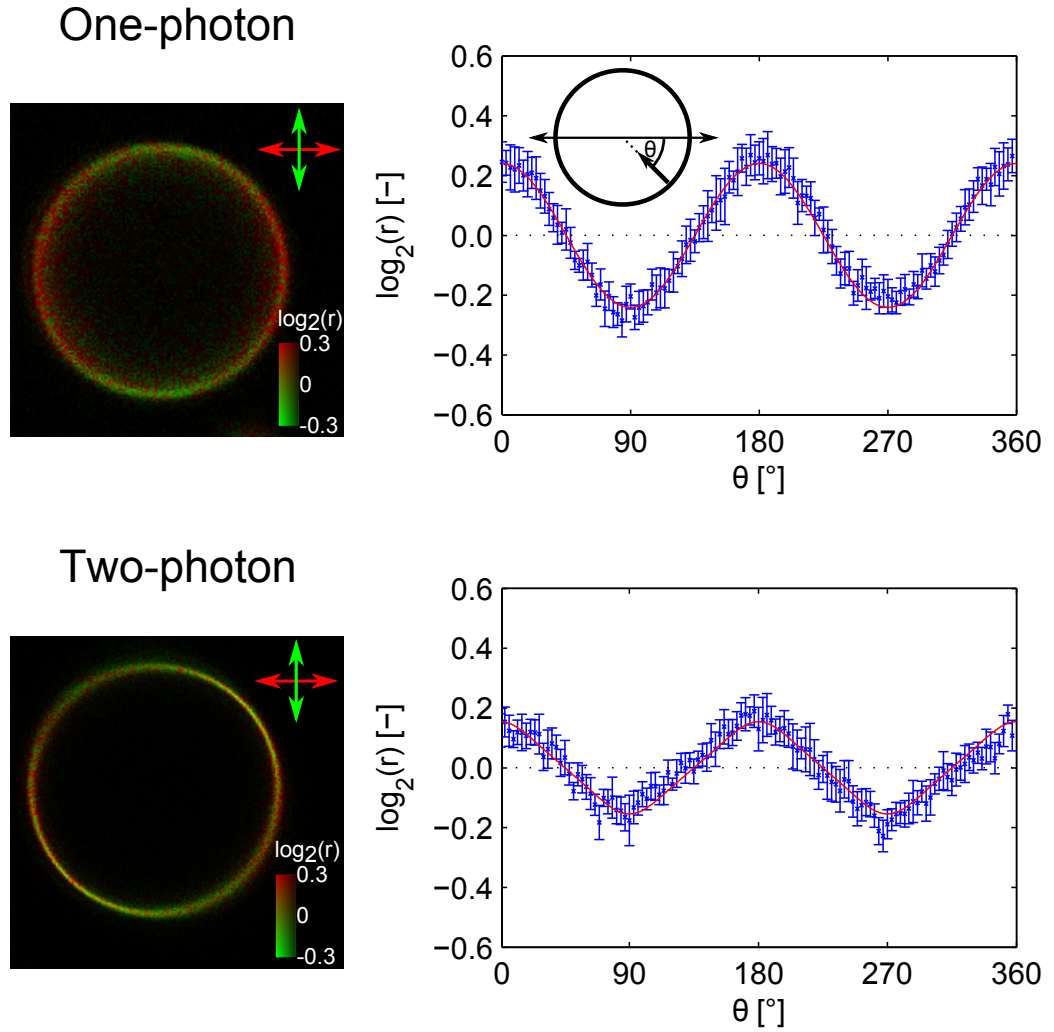


Figure 1.6: 1P and 2P linear dichroism of the F2N12S probe in POPC GUVs. We depict images of representative GUVs (left) and plots showing the dependence of the logarithm of the dichroic ratio r on the orientation of the membrane normal (right). The error bars correspond to the 95% confidence intervals, and the red curves represent the theoretical model based on (1.12)–(1.15) fitted to the experimental data.

$\langle \cos^2 \alpha \rangle$	$\langle \cos^4 \alpha \rangle$	$\langle P_2 \rangle$	$\langle P_4 \rangle$
0.372 ± 0.001	0.181 ± 0.002	0.057 ± 0.002	-0.211 ± 0.010

Table 1.1: Orientational distribution parameters with their 95 % confidence intervals obtained by fitting a combination of 1P and 2P experimental data on the F2N12S probe in POPC GUVs.

of $\log_2 r$ lied around 0.15 (i.e., $r = 1.11$). Images of typical GUVs are shown in Figure 1.6 together with the dependence of $\log_2 r$ on the orientation of the bilayer normal. By fitting 1P and 2P experimental data with functions based on (1.12)–(1.15), we were able to determine values of $\langle \cos^2 \alpha \rangle$ and $\langle \cos^4 \alpha \rangle$ and their 95 % confidence intervals. These values together with those of $\langle P_2 \rangle$ and $\langle P_4 \rangle$ can be found in Table 1.1.

The parameters gained from the fit were utilized for finding estimates of the tilt angle distribution based on the three approaches discussed in the previous section. First, we found that $\langle \cos^2 \alpha \rangle$ and $\langle \cos^4 \alpha \rangle$ of $F_{Gauss}(\alpha)$ belonged to the experimentally determined confidence intervals for Gaussian functions $f_{Gauss}(\alpha)$ with α_0 within $(50.0, 50.3)^\circ$ and σ within $(192.2 - 3.52\alpha_0, 192.8 - 3.53\alpha_0)^\circ$. Second, the values of $\langle P_2 \rangle$ and $\langle P_4 \rangle$ presented in Table 1.1 enabled us to construct a distribution function $F_{Leg}(\alpha)$ from the truncated Legendre expansion $f_{Leg}(\alpha)$. Finally, by substituting the values of $\langle P_2 \rangle$ and $\langle P_4 \rangle$ presented in Table 1.1 into (1.29) and (1.30) and solving the resulting set of nonlinear equations, we calculated the Lagrange multipliers in $f_S(\alpha)$ as $\lambda_2 = 0.13 \pm 0.04$ and $\lambda_4 = -2.4 \pm 0.3$. All the three different estimates $F_{Gauss}(\alpha)$, $F_{Leg}(\alpha)$, and $F_S(\alpha)$ of the tilt angle distribution are compared in Figure 1.7. We notice that $F_{Leg}(\alpha)$ has the lowest and broadest peak of all the three distributions but becomes negative for lower values of α . On the other hand, the peak of $F_S(\alpha)$ is the highest and narrowest one, but in contrast to the other two distributions, $F_S(\alpha)$ possesses a more pronounced tail in the region of high α .

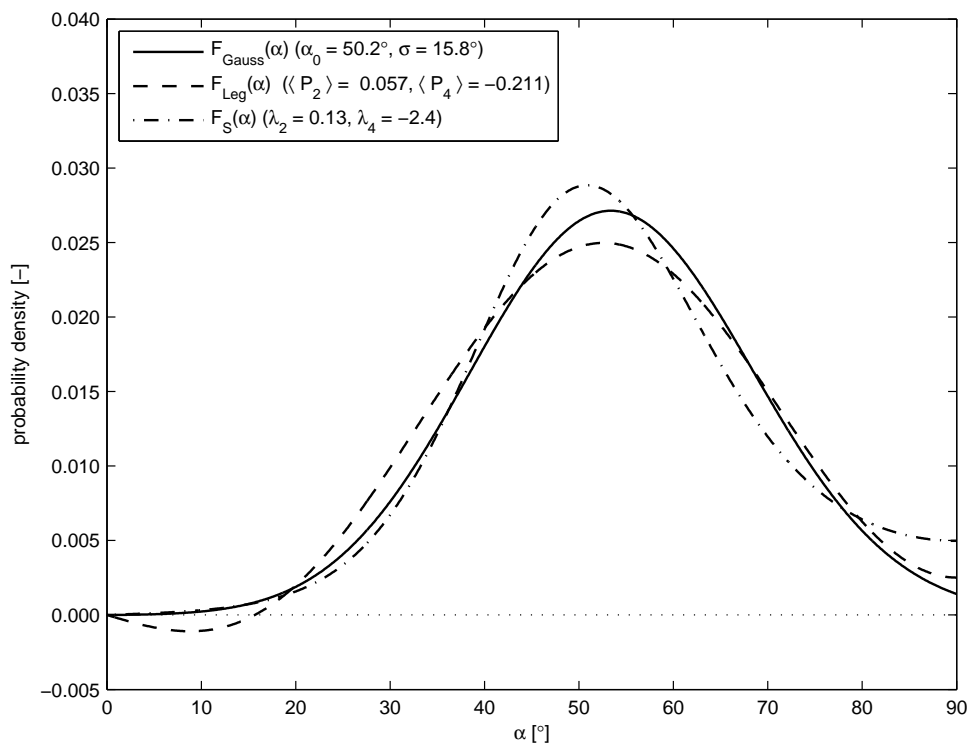


Figure 1.7: Estimates of the orientational distribution reconstructed from a combination of 1P and 2P linear dichroism measurements of the F2N12S probe in POPC GUVs.

2. Molecular Dynamics

In this chapter, we introduce the general ideas behind classical molecular dynamics and review the current progress in simulations of fluorescent probes. Next, we describe the parametrization of our system of interest and our simulation protocol. Finally, we analyze simulation results.

2.1 Classical Molecular Dynamics

Molecular dynamics (MD) is a computer simulation of motions of atoms and molecules. Classical MD simulates the temporal behavior of a system of atoms and molecules by numerically solving the classical equations of motion. The instantaneous state of a system containing N atoms at time t is described by N position vectors $\mathbf{r}_i(t)$ and N velocity vectors $\mathbf{v}_i(t)$. The equations governing the dynamics of each of the atoms are simply Newton's equations of motion,

$$\frac{d\mathbf{r}_i}{dt} = \mathbf{v}_i(t), \quad (2.1)$$

$$m_i \frac{d\mathbf{v}_i}{dt}(t) = \mathbf{F}_i(\mathbf{r}_j, t). \quad (2.2)$$

Newton's equations of motion are solved using finite differences methods (Allen and Tildesley, 1989), with a finite time step Δt . Integrating Newton's equations numerically in a straightforward way as

$$\mathbf{r}_i(t + \Delta t) = \mathbf{r}_i(t) + \mathbf{v}_i(t)\Delta t + \frac{1}{2} \frac{\mathbf{F}_i(t)}{m_i} (\Delta t)^2, \quad (2.3)$$

$$\mathbf{v}_i(t) = \mathbf{v}_i(t - \Delta t) + \frac{\mathbf{F}_i(t)}{m_i} \Delta t, \quad (2.4)$$

leads to numerically irreversible propagation of the system in time, which is not desirable, since time reversibility is an intrinsic property of Newton's equations of motion. Therefore, different schemes maintaining time reversibility have been developed to numerically integrate Newton's equations of motion, such as the Verlet propagator (Verlet, 1967), which calculates new positions on the basis of the positions at two previous times,

$$\mathbf{r}_i(t + \Delta t) = 2\mathbf{r}_i(t) - \mathbf{r}_i(t - \Delta t) + \frac{\mathbf{F}_i(t)}{m_i} (\Delta t)^2, \quad (2.5)$$

without requiring an explicit calculation of velocities, or the leap frog propagator (Hockney et al., 1974), which alternates evaluating velocities and positions,

$$\mathbf{v}_i(t + \frac{1}{2}\Delta t) = \mathbf{v}_i(t - \frac{1}{2}\Delta t) + \frac{\mathbf{F}_i(t)}{m_i} \Delta t, \quad (2.6)$$

$$\mathbf{r}_i(t + \Delta t) = \mathbf{r}_i(t) + \mathbf{v}_i(t + \frac{1}{2}\Delta t)\Delta t. \quad (2.7)$$

Other propagators used include the velocity Verlet propagator (Swope et al., 1982) or the Gear predictor–corrector propagator (Allen and Tildesley, 1989).

The forces $\mathbf{F}_i(t)$ are calculated from a potential function $V(\mathbf{r}_j)$ as

$$\mathbf{F}_i(t) = -\frac{\partial V}{\partial \mathbf{r}_i}(\mathbf{r}_j(t)). \quad (2.8)$$

The potential function comprises bonded, nonbonded, and restraint terms (van der Spoel et al., 2010). Bonded terms describe covalent-bond stretching, angle bending, dihedral rotation, and improper dihedrals. Bond stretching is mostly represented by a harmonic potential

$$V_{bond}(r_{ij}) = \frac{1}{2}k^{ij}(r_{ij} - r_{ij}^0)^2. \quad (2.9)$$

A harmonic potential is also used to describe angle bending,

$$V_{ang}(\theta_{ijk}) = \frac{1}{2}k^{ijk}(\theta_{ijk} - \theta_{ijk}^0)^2, \quad (2.10)$$

sometimes complemented by a harmonic Urey-Bradley potential between the atoms i and k on the opposite sides of the angle. Dihedral rotation is typically represented by several terms of a cosine potential

$$V_{dih}(\phi_{ijkl}) = \sum_n k_n^{ijkl}(1 + \cos(n\phi_{ijkl} - \phi_n^{ijkl})) \quad (2.11)$$

or, alternatively, by the Ryckaert-Bellemans function

$$V_{dih}(\phi_{ijkl}) = \sum_{n=0}^5 C_n^{ijkl}(\cos(\phi_{ijkl} - 180^\circ))^n. \quad (2.12)$$

Improper dihedral potentials are intended, e.g., to maintain planarity of rings and their substituents. They are mostly used in form of a harmonic potential or the cosine potential (2.11). Nonbonded terms include the Coulomb interaction

$$V_{coul}(r_{ij}) = \frac{1}{4\pi\epsilon_0\epsilon_r} \frac{q_i q_j}{r_{ij}} \quad (2.13)$$

and the van der Waals interaction, modeled typically using the Lennard-Jones potential

$$V_{len}(r_{ij}) = \left(\frac{C_{12}^{ij}}{r_{ij}} \right)^{12} - \left(\frac{C_6^{ij}}{r_{ij}} \right)^6. \quad (2.14)$$

Atoms participating in the same bonded interaction are excluded from all mutual nonbonded interactions. An exception can be the first and fourth atoms in a dihedral, which are sometimes assigned an extra 1–4 pair interaction described by an electrostatic or van der Waals term. Finally, various restraint potentials can be used to restrain positions, angles, dihedrals, and distances of atoms or atom groups.

The functional form of the terms in $V(\mathbf{r}_j)$ together with all the parameters establish a force field. There are a number of available force fields. For membrane simulations, the most frequently used ones are based on the GROMOS force field (Hermans et al., 1984; Schuler et al., 2001; Chandrasekhar et al., 2003) or the CHARMM force fields (MacKerell et al., 1995, 1998; Feller and MacKerell, 2000). The GROMOS force field treats each CH, CH₂, and CH₃ group as a single particle. This is called a united-atom approach. In contrast, the CHARMM force field describes all hydrogen atoms explicitly. Another force field used, although less frequently, in membrane simulations is the AMBER force field (Wang et al., 2004; Jojart and Martinek, 2007). The performance of these force fields in membrane simulations compared to experiments is discussed in detail in (Lyubartsev and Rabinovich, 2011).

A modification of the GROMOS force field widely used in membrane simulations, known as the Berger lipids force field, was developed by (Berger et al., 1997). It describes valence-bond stretching, angle bending, and improper dihedrals, as well as the rotation of the dihedrals in the phospholipid head group region using parameters of the GROMOS force field, but in contrast to GROMOS, it employs the Ryckaert-Bellemans functions (2.12) to model the dihedral potentials of the hydrocarbon chains. In addition, it adopts the Lennard-Jones parameters from the OPLS force field (Jorgensen and Tirado-Rives, 1988), often used in protein simulations, and includes a modified set of atomic charges (Chiu et al., 1995).

The number of atoms in a simulation is limited by the rapidly growing computational cost when increasing the system size. Therefore, periodic boundary conditions (PBC) are used in simulations of condensed phase to reduce the computational cost (Allen and Tildesley, 1989). The simulated system is contained in a box which is replicated in three (or two) dimensions. If an atom leaves the central box, it immediately enters the box on its opposite side.

To further decrease the computational cost, nonbonded interactions are trun-

cated at a certain cutoff distance (Allen and Tildesley, 1989). To reduce energy fluctuations resulting from the step in the interaction potential at the cutoff distance, switching or shifting functions are often used, which bring the potential smoothly to zero. Interaction cutoff works well for the relatively short-ranged Lennard Jones potential but can cause a significant error when used with the Coulomb interaction, which decays slowly as $1/r$. Therefore, the Ewald summation (Ewald, 1921), originally proposed for calculation of long-range interactions in crystals, is used to evaluate the Coulomb interaction. Its idea is to decompose the Coulomb potential into a short-range and a long-range part. While a cutoff can be applied to the quickly decaying short-range part, the Fourier transform of the long-range part is easily summed in the reciprocal space. An improved version of the original Ewald summation is the particle-mesh Ewald method (Darden et al., 1993; Essmann et al., 1995).

Coarse-grained force fields, such as the MARTINI force field (Marrink et al., 2007), allow simulation of much bigger systems than their all-atom and united-atom counterparts. Coarse-grained force fields combine several atoms into one ball, or bead. Consequently, the significantly increased system size is at the expense of atomic resolution.

Different statistical ensembles can be sampled by MD (Allen and Tildesley, 1989; Chandler, 1987). The simplest ensemble is the microcanonical (NVE) ensemble, which keeps the number of atoms, box volume, and the total energy constant. More realistic ensembles for most experiments include the isothermal (NVT) ensemble, fixing the number of atoms, box volume, and temperature, and the isothermal–isobaric (NPT) ensemble, maintaining a constant number of atoms, pressure, and temperature. For systems with a variable number of atoms, grandcanonical (μVT) ensemble can be used, which fixes the chemical potential, volume, and temperature. Temperature is kept at a given value by a thermostat. Commonly used thermostats include the Berendsen thermostat (Berendsen et al., 1984), which scales velocities of all atoms at each step by a variable factor, the Andersen thermostat (Andersen, 1980), which assigns randomly selected atoms with velocities chosen from the Maxwell-Boltzmann distribution, and the Nosé-Hoover thermostat (Hoover, 1985), which adds a virtual degree of freedom with its own equation of motion to the system’s existing degrees of freedom. Analogously to thermostats, barostats are used to control the system’s pressure. The Berendsen barostat (Berendsen et al., 1984) scales atomic coordinates and the dimensions of the box at every step, while the Parrinello-Rahman barostat (Parrinello and Rahman, 1981; Nosé and Klein, 1983) operates on a similar principle as the Nosé-Hoover thermostat.

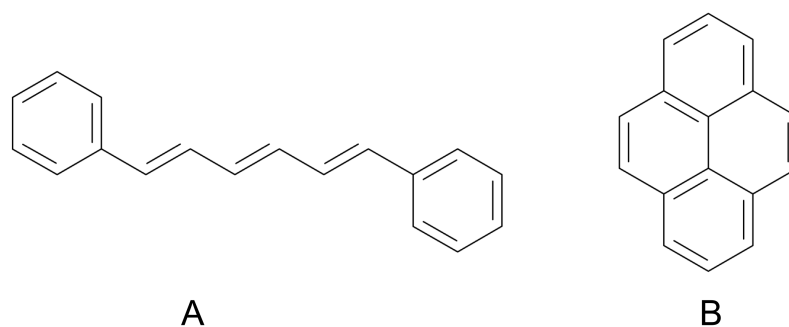


Figure 2.1: Structures of (A) DPH and (B) pyrene. Adapted from (Loura and Ramalho, 2011).

2.2 Molecular Dynamics of Fluorescent Probes

Fluorescent techniques are widely employed to study properties of lipid membranes. The function of fluorescent probes as reporters on the membrane environment critically depends on their location and orientation within the membrane as well as on to what extent these probes perturb membrane properties. Unfortunately, this information is often not accessible by experiments. MD, which presents a powerful tool to answer these questions, has been used to examine a number of fluorescent probes over the past two decades (Loura and Ramalho, 2011; Loura et al., 2012).

The first probes to be studied were small nonpolar molecules, such as DPH (Figure 2.1A) or pyrene (Figure 2.1B). Fluorescence anisotropy of DPH has been commonly employed by experimentalists to measure membrane microviscosity, but the orientation of DPH relative to the membrane normal long remained unclear. The first MD simulation of DPH (Cascales et al., 1997) used a modified GROMOS force fields but was limited by a very short sampling time of 250 ps. Later works (Repáková et al., 2004, 2005), utilizing the Berger lipids force field to describe both the lipids and the nonpolar probe, achieved substantially longer simulation times (up to 100 ns), which allowed them to investigate the orientation of DPH as well as its location and dynamics in the membrane. The most recent paper (Fraňová et al., 2010) studied the effect of cholesterol on the orientational distribution of DPH in lipid bilayers. A study (Hoff et al., 2005) of pyrene, which is known for its long fluorescence lifetime and a tendency to form excimers, compared MD results on the orientation of pyrene with data from NMR. Papers (Repáková et al., 2006; Čurdová et al., 2007) investigated the effect of pyrene-labeled phospholipids on the structural properties of a lipid membrane, in the latter case simulating the membrane not only in the liquid phase but also in the

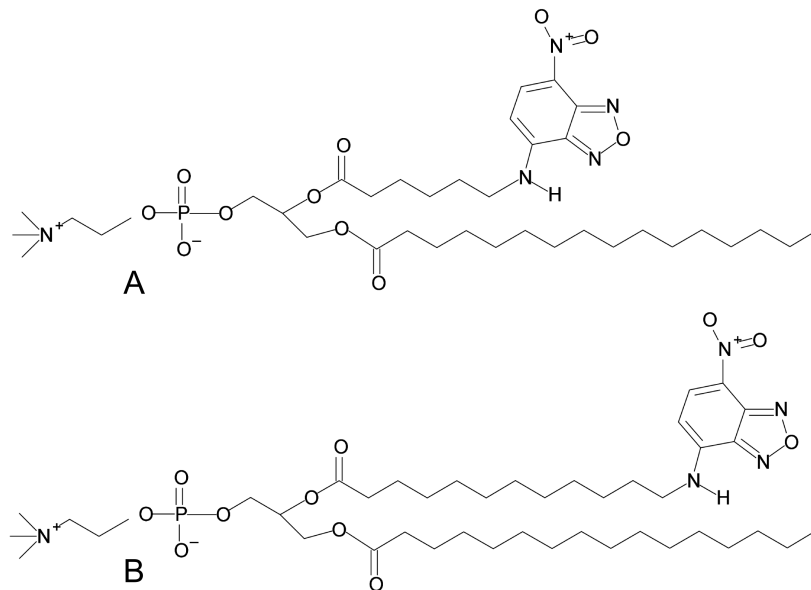


Figure 2.2: Structures of (A) C6-NBD-PC and (B) C12-NBD-PC. Adapted from (Loura and Ramalho, 2011).

gel phase. All the three papers used the Berger lipids force field to parametrize the simulated systems.

In recent years, the focus has shifted to simulations of larger polar fluorophores, which should be carefully parametrized in order to describe the complex nature of their interactions with the membrane environment. C6-NBD-PC and C12-NBD-PC (Figure 2.2), phospholipids with fluorophore-labeled fatty acid chains used as fluorescent analogs of lipids in biological and model membranes, were simulated by (Loura and Ramalho, 2007; Loura et al., 2008, 2010). The authors employed the Berger lipids force field for lipid parametrization, but they obtained the geometry and charges of the NBD fluorophore from quantum calculations. BODIPY-PC (Figure 2.4A), another phospholipid with a fluorophore-labeled fatty acid chain, was modeled by (Song et al., 2011) with the use of the CHARMM force field. Head-group labeled phospholipids present another category of polar fluorescent probes that have been investigated with the help of MD. These probes have a potential to introduce less disturbance to the lipid membrane than phospholipids with fluorophore-labeled fatty acid chains. For example, the Texas Red-DHPE probe (Figure 2.3A), used to study phase behavior of lipid mixtures, was simulated by (Skaug et al., 2009). The parametrization of the system was based on the Berger lipids force field, but atomic charges were assigned to the Texas Red fluorophore and the DHPE head group on the basis of quantum calculations. Rhodamine-DPPE (Figure 2.3B), a similar head-group labeled phospholipid, with the force field parameters assigned analogously to the previous case, was simulated by (Kyrychenko, 2010). Other probes exam-

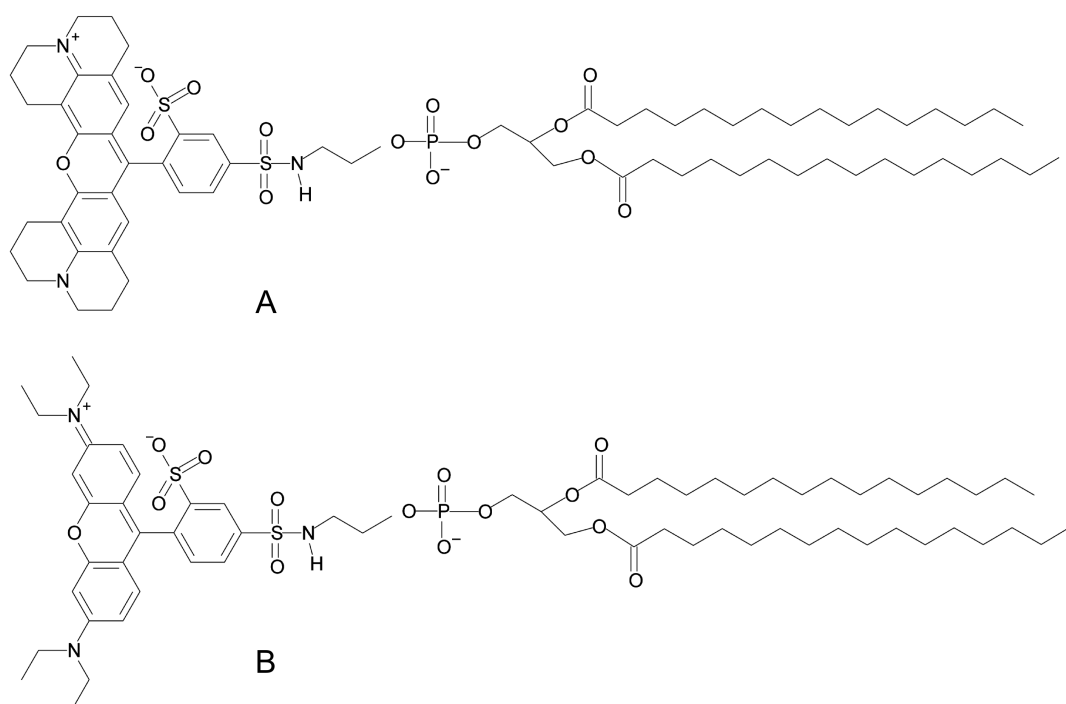


Figure 2.3: Structures of (A) Texas Red-DHPE and (B) Rhodamine-DPPE. Adapted from (Loura and Ramalho, 2011).

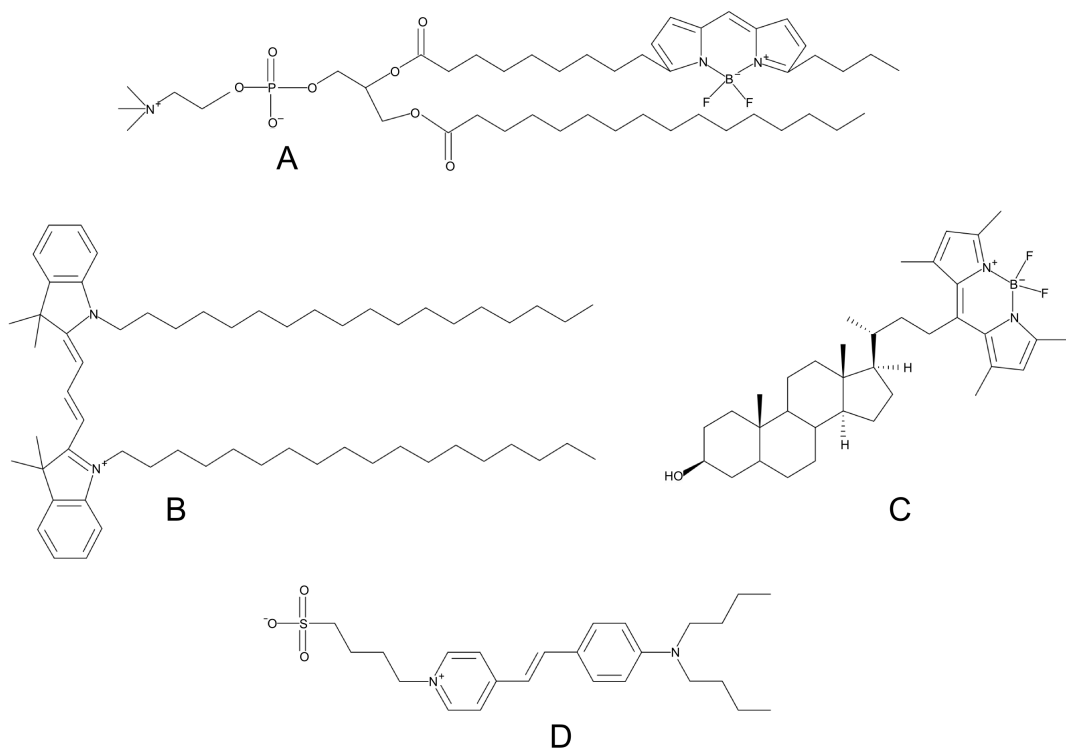


Figure 2.4: Structures of (A) BODIPY-PC, (B) DiIC₁₈(3), (C) BODIPY-cholesterol, and (D) Di-4-ASPBS. Adapted from (Loura et al., 2012).

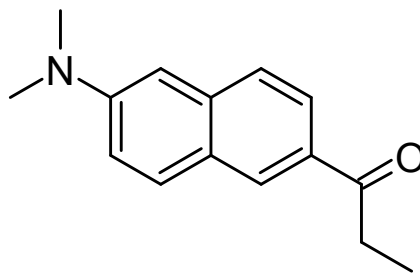


Figure 2.5: Structure of PRODAN.

ined using MD include DiIC₁₈(3) (Gullapalli et al., 2008; Muddana et al., 2011), a carbocyanine-based dye (Figure 2.4B) sensitive to membrane potential, and BODIPY-cholesterol (Holtta-Vuori et al., 2008) (Figure 2.4C), which is used to measure membrane partitioning of cholesterol. In (Cwiklik et al., 2011), the authors investigated the behavior of the S₁ excited state of the PRODAN probe (Figure 2.5) in a phospholipid bilayer and the absorption and emission spectra of the probe in the membrane environment. Finally, coarse-grained simulations of the voltage sensitive Di-4-ASPBS dye (Figure 2.4D) and its derivatives were performed using the MARTINI force field by (Hinner et al., 2009).

2.3 Probe Parametrization and Simulation Protocol

In order to construct force field parameters for the F2N12S probe, we first performed quantum geometry optimization of the fluorophore with a shorter four-carbon alkyl chain in place of the original twelve-carbon chain. We used the Gaussian 09 program (Frisch et al., 2009) and employed the B3LYP functional (Becke, 1993) with the cc-pVDZ basis set (Dunning, 1989). After cutting off the terminal CH₃ group of the shortened alkyl chain and adding the missing nine CH_n groups, we used the PRODRG2 server (Schuttelkopf and van Aalten, 2004) to generate a GROMACS topology file based on the united-atom GROMOS-87 force field (van Gunsteren and Berendsen, 1987) with corrections as detailed in (van Buuren et al., 1993; Mark et al., 1994) (originally referred to as the GROMACS force field). The atom names of the F2N12S probe are shown in Figure 2.6. To ensure proper interactions with membrane lipids, the default CH2 and CH3 united-atom types of the twelve-carbon alkyl chain were replaced with the LP2 and LP3 atom types adopted from the united-atom Berger lipids force

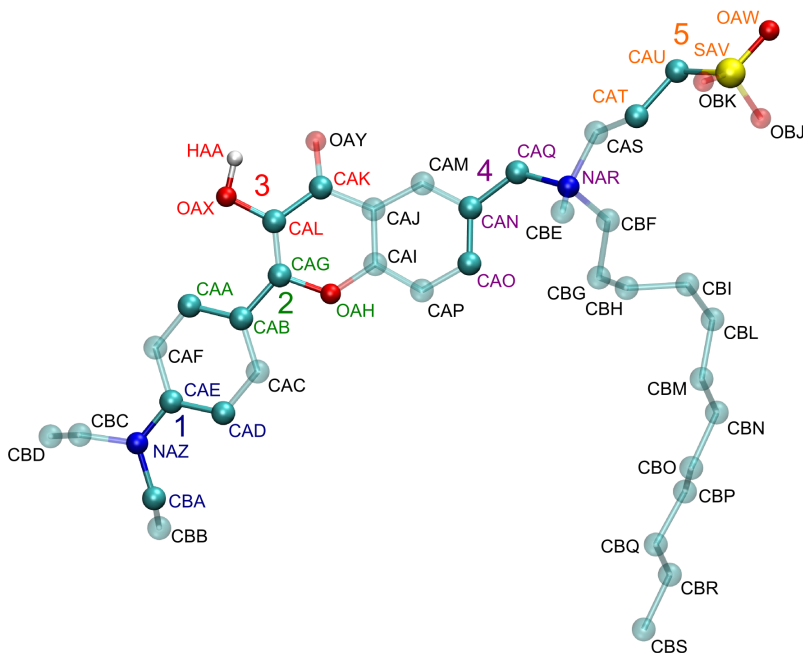


Figure 2.6: Atom names of the F2N12S probe and dihedrals (1–5) parametrized using quantum calculations. Color coding: cyan, carbon; red, oxygen; white, hydrogen; blue, nitrogen; yellow, sulfur.

field. Atomic charges of the fluorophore were obtained from the Merz-Kollman electrostatic potential fit (Singh and Kollman, 1984) for the optimized structure. The groups treated as united atoms were assigned charges equal to the sums of those of their constituents. The nine terminal CH_n groups of the twelve-carbon alkyl chain were given a zero charge, in accord with the Berger lipids force field, and the charges of the second and the third CH_2 groups of the twelve-carbon alkyl chain were decreased by a small value of $0.03 e$ to make the whole structure neutral. The atom types of the GROMOS-87 and the Berger lipids force fields assigned to the atoms of the F2N12S probe together with the atomic charges and charge groups are shown in Table 2.1. Furthermore, five dihedrals of the F2N12S probe (see Figure 2.6) were parametrized on the basis of quantum calculations. Rigid scans of the dihedral potentials were carried out on molecular fragments (shown in Figure 2.7) by employing the B3LYP functional with the cc-pVDZ basis set. After subtraction of the Coulomb and Lennard-Jones contribution, the obtained potentials were fitted with a sum of the first four terms of the periodic cosine potential (2.11). The resulting parameters k_n^{ijkl} and ϕ_n^{ijkl} ($n = 1, \dots, 4$) can be found in Table 2.2. Regarding the rest of the system, POPC molecules were described using the Berger lipids force field and water with the SPC model (Berendsen et al., 1981).

Classical MD simulations were performed using the program GROMACS 4.5.2 (van der Spoel et al., 2010). A periodic box containing a single F2N12S molecule, 128 POPC molecules forming a bilayer, and 8952 water molecules was simulated. Four different sets of initial conditions were prepared with the dye molecule inserted into the vicinity of the membrane, and with its alkyl chain being either inside or outside the bilayer. After energy minimization and a fast 10 ns equilibration period, 500 ns runs were performed at constant pressure and temperature for each set of initial conditions. A time step of 2 fs was employed. Temperature of 310 K, slightly increased in comparison to the experiments to speed up sampling, was maintained by the Nosé-Hoover thermostat with a time constant $\tau_T = 1$ ps, and the pressure was kept at 1.01 bar by the Parrinello-Rahman barostat with a time constant $\tau_p = 2$ ps. The LINCS algorithm (Hess et al., 1997) was employed for constraining the bond lengths of F2N12S and POPC molecules, while the bond lengths of water molecules were constrained with the SETTLE algorithm (Miyamoto and Kollman, 1992). The non-bonded interaction cutoff was set to 1 nm, and the long-range electrostatic interactions were accounted for using the particle-mesh Ewald method with grid spacing of 0.12 nm and fourth-order interpolation.

atom	atom type	charge (units of e)	charge group
CBS	LP3	0	1
CBR	LP2	0	2
CBQ	LP2	0	3
CBP	LP2	0	4
CBO	LP2	0	5
CBN	LP2	0	6
CBM	LP2	0	7
CBL	LP2	0	8
CBI	LP2	0	9
CBH	LP2	0.12	10
CBG	LP2	0.07	10
CBF	LP2	-0.09	11
NAR	NL	0.02	11
CAS	CH2	0.07	11
CAT	CH2	0.17	11
CAU	CH2	-0.1	12
SAV	S	1.01	12
OBJ	OM	-0.54	12

continued on next page

atom	atom type	charge (units of e)	charge group
OBK	OM	-0.6	12
OAW	OM	-0.58	12
CBE	CH3	0.2	11
CAQ	CH2	0.16	11
CAN	CB	-0.04	13
CAM	CR61	0.11	13
CAO	CR61	0.17	13
CAP	CR61	-0.16	13
CAI	CB	0.4	14
OAH	OS	-0.22	14
CAJ	CB	-0.31	14
CAK	CB	0.44	15
OAY	O	-0.49	15
CAL	CB	0.04	16
OAX	OA	-0.44	16
HAA	HO	0.37	16
CAG	CB	0.09	14
CAB	CB	0.03	17
CAC	CR61	0.02	17
CAD	CR61	-0.16	17
CAA	CR61	0.07	17
CAF	CR61	-0.19	17
CAE	CB	0.42	18
NAZ	N	-0.41	18
CBC	CH2	0.24	18
CBD	CH3	-0.04	19
CBA	CH2	0.23	18
CBB	CH3	-0.04	20

Table 2.1: Atom types of the GROMOS-87 and Berger lipids force fields, atomic charges, and charge groups used to parametrize the F2N12S probe.

dih. No.	k_1^{ijkl}	ϕ_1^{ijkl}	k_2^{ijkl}	ϕ_2^{ijkl}	k_3^{ijkl}	ϕ_3^{ijkl}	k_4^{ijkl}	ϕ_4^{ijkl}
1	0.00	180.00	39.55	182.07	0.36	180.00	2.77	180.00
2	1.55	0.00	23.87	180.10	0.26	0.00	1.02	183.57
3	19.10	182.68	4.02	169.34	6.47	185.04	-1.69	188.64
4	1.56	142.60	13.28	182.93	0.73	63.65	4.03	185.64
5	2.07	45.26	-0.37	60.19	14.53	11.82	-0.34	-78.73

Table 2.2: Values of dihedral parameters obtained from quantum scans. Parameters k_n^{ijkl} are in kJ/mol and ϕ_n^{ijkl} in degrees.

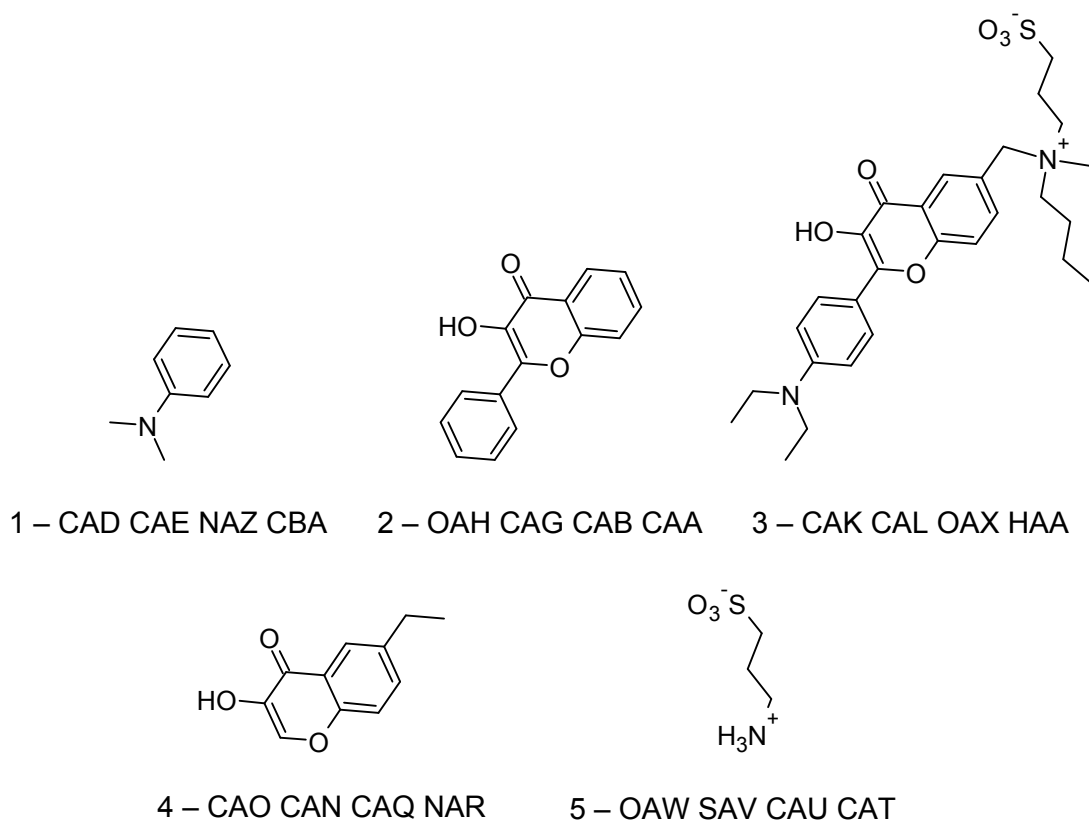


Figure 2.7: Fragments used for dihedral parametrization.

2.4 Trajectory analysis

All four MD runs started with the aromatic rings of the probe placed at the membrane–water interface (Figure 2.8A). In one case, the probe was anchored to the membrane with its twelve-carbon alkyl chain, while in the remaining three cases, the alkyl chain was freely floating in the water environment. Regardless of the particular initial conditions, we observed stabilization of the probe within the membrane no later than 150 ns after the start of the simulations. In two cases, the relocation proceeded through an intermediate state characterized by the aromatic rings being located in the polar part of the bilayer, the twelve-

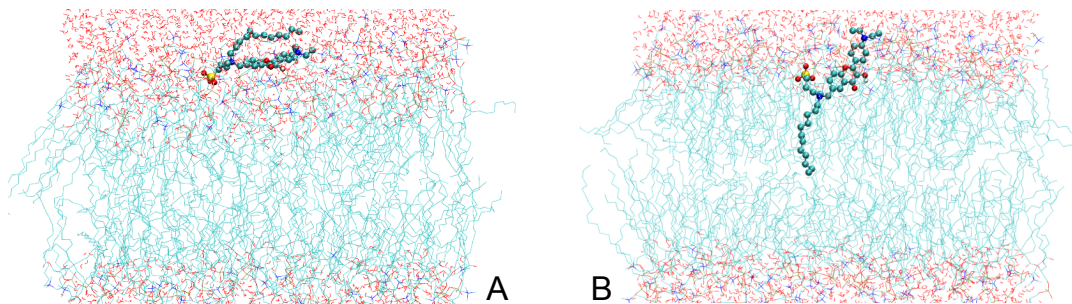


Figure 2.8: One of the initial states (A) and an intermediate state (B).

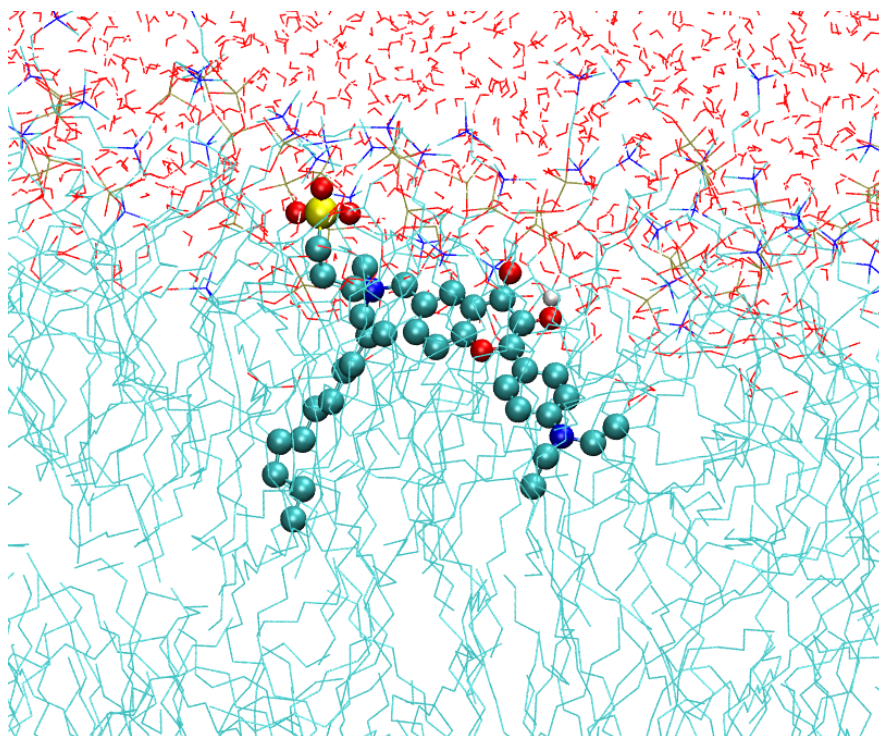


Figure 2.9: A typical snapshot from MD.

carbon alkyl chain embedded in the hydrophobic core of the membrane, and the diethylamine group pointing out of the membrane to the water environment (Figure 2.8B). Ultimately, the aromatic rings adopted a tilted orientation with the diethylamine group directed towards the center of the bilayer, the SO_3^- group held in the polar part of the membrane, and the twelve-carbon alkyl chain located among acyl chains of the POPC molecules. Figure 2.9 shows a typical probe location in the bilayer.

The last 300 ns of each of the 500 ns simulations were used for further analysis. We started by examining the average distances of several of the probe's atoms and groups from the bilayer center. The density profiles of these atoms and groups together with those of the POPC choline nitrogen, phosphate phosphorus, sn-1 and sn-2 carbonyl oxygen atoms (see Figure 1.2), and water are summarized in Figure 2.10. We found that, on average, the probe's ammonium nitrogen, to which

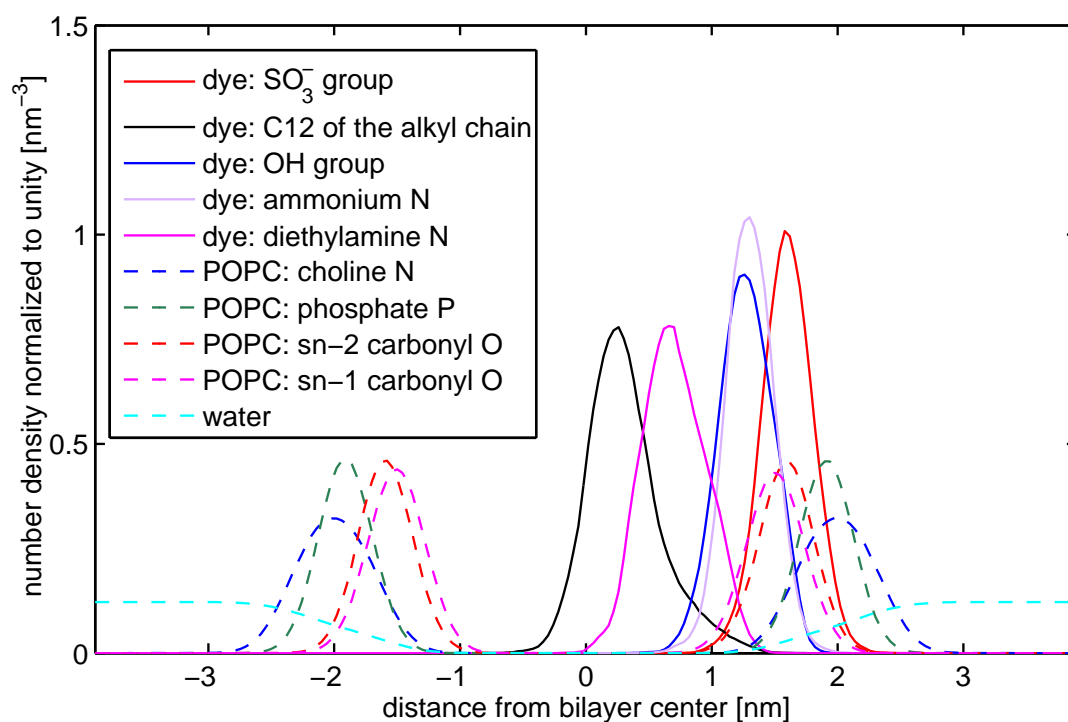


Figure 2.10: Total density profiles of selected atoms and groups of the system as a function of the distance from the bilayer center.

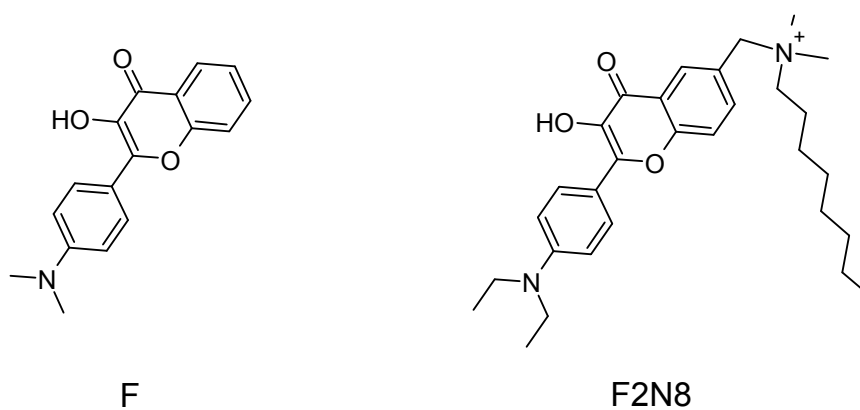


Figure 2.11: Probes F (left) and F2N8 (right).

the twelve-carbon alkyl chain is attached, was located slightly below the level of the sn-1 and sn-2 carbonyl oxygen atoms, at a distance of 1.30 nm from the bilayer center. The other nitrogen of the probe was located considerably lower, with its density profile peaking at 0.65 nm from the center of the bilayer. The density profile of the OH group attained its maximum at 1.25 nm, close to the peak of the ammonium nitrogen. The maximum of the SO_3^- group lied at 1.60 nm, i.e. at the same level as the sn-2 carbonyl oxygen and below the peaks of the POPC phosphorus and nitrogen atoms. Nevertheless, a more detailed inspection reveals that the choline head groups of the neighboring POPC molecules can tilt down to interact with SO_3^- . Finally, the terminal carbon atom of the twelve-carbon alkyl chain exhibited a broad density profile with a peak at 0.25 nm, i.e., close to the bilayer center. Overall, we observed the average location of the probe to be deeper than expected by (Shynkar et al., 2007). Illustrating the expected location of the probe in a phospholipid bilayer, the authors placed the ammonium nitrogen only slightly below the phosphate group, the other nitrogen somewhat below the sn-1 carbonyl oxygen, and the SO_3^- group up to the membrane–water interface.

The carbonyl groups of 3-hydroxyflavone-based probes can form hydrogen bonds with water. Analysis of emission spectra of 3-hydroxyflavone-based probes embedded in phospholipid bilayers reveals that both the hydrated and nonhydrated forms are present, their exact ratio being dependent on lipid composition and temperature. For a small 3-hydroxyflavone-based probe F, sharing the same aromatic rings with the F2N12S probe but complemented with only a dimethylamino group (Figure 2.11), distinct locations of its hydrated and nonhydrated forms were reported (Klymchenko et al., 2004a). The hydrated form was found to reside in the polar part of the bilayer, close to the membrane-water interface, while the nonhydrated forms was buried in the hydrophobic region of the bilayer. To learn whether the F2N12S probe exhibits a similar bimodality, we analyzed the contacts of the probe’s carbonyl oxygen with water. The criterion for the existence of a contact was based on the distance of the water oxygen from the carbonyl oxygen, which should not exceed 3.5 Å. We investigated the fraction of time the carbonyl oxygen spent in contact with water as a function of the distance of the carbonyl oxygen from the bilayer center. We found a clear rise in contacts with a growing distance from the center of the bilayer (Figure 2.12A), corresponding to the increased hydration of the bilayer in its shallower regions. However, plotting the fraction of time spent in contact with water relative to the location of the probe’s center of mass (Figure 2.12C) revealed a less pronounced increase, indicating that the hydrated and nonhydrated forms differed rather by the tilt of the aromatic rings than by the depth of the probe as a whole. This is consistent with experimental results (Klymchenko et al., 2004b) obtained for

the F2N8 probe (Figure 2.11), which bears closer similarity to F2N12S than the small probe F.

To gain more detailed information on interactions of the F2N12S probe embedded in the bilayer, apart from the contacts between the probe’s carbonyl oxygen and water, we analyzed the existence of contacts between the heterocycle oxygen of the probe and water, between the probe’s OH group and sn-1 and sn-2 ester oxygen atoms, the OH group and sn-1 and sn-2 carbonyl oxygen atoms, the OH group and phosphate, and finally, between the OH group and water. The results are summarized in Figure 2.13. While there were virtually no contacts between the heterocycle oxygen of the probe and water, we found the probe’s OH group to spend a significant amount of time in contacts with the sn-1 and sn-2 ester oxygen atoms and with the sn-1 carbonyl oxygen.

Besides the overall analysis combining data from the four MD runs, we also divided the trajectories into a total of twelve 100 ns parts and conducted analysis separately for each of them. The results of the contact analysis are shown in Figure 2.14. There are significant differences between the individual parts, most notably between parts 1a–1c and the remaining ones. This was caused by a different orientation of the probe’s carbonyl and OH groups in one of the simulation runs. While during the other three runs, these groups were constantly pointing to the membrane–water interface, in this particular case, they stayed oriented toward the bilayer center and were thus prevented from interacting with water and polar lipid head groups. The differences among the individual parts convey important information on the dynamics of polar molecules embedded in lipid membranes, suggesting that it takes a relatively long time for a polar molecule to explore all the possible locations and interactions in the anisotropic membrane environment.

Nevertheless, the primary interest of the present work is a comparison of the orientational distribution of the 1P TDM reconstructed from LD measurements with that determined by simulations. To see how the above mentioned slow sampling affects convergence of the 1P TDM orientational distribution, we first need to obtain information on the direction of the 1P TDM relative to the probe’s molecular geometry. This is a subject of the next chapter.

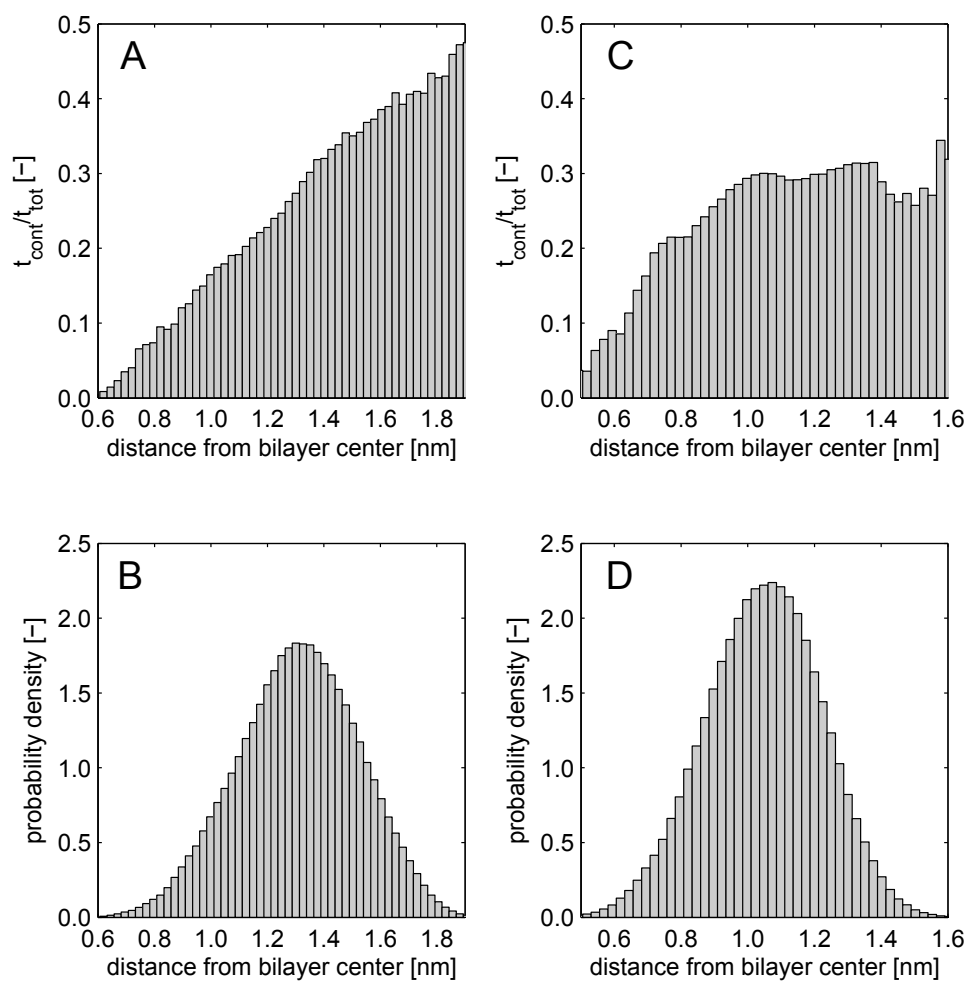


Figure 2.12: Fraction of total simulation time spent by the carbonyl oxygen of the probe in contact with water depending (A) on the atom's distance from the bilayer center and (C) on the distance of the probe's center of mass from the bilayer center. The corresponding density profiles of the carbonyl oxygen (B) and the center of mass (D) are also shown.

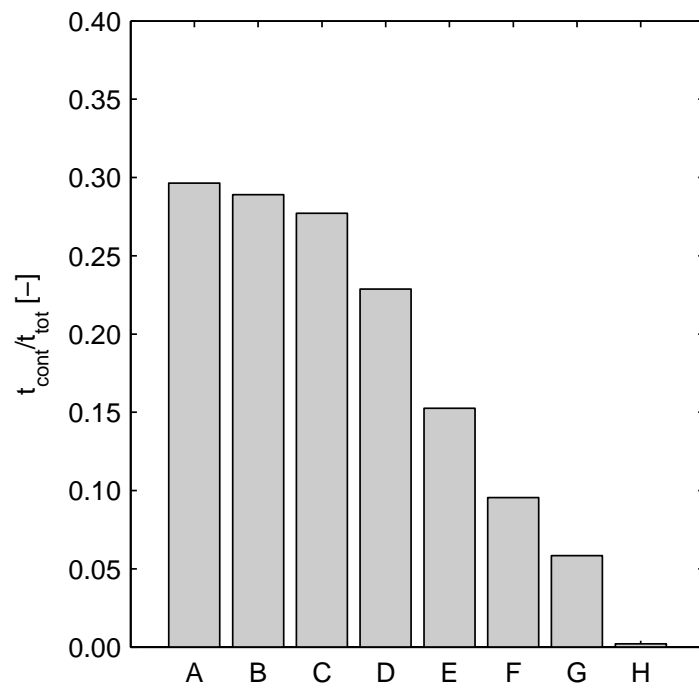


Figure 2.13: Fraction of total simulation time spent by selected atoms or groups of the probe in contact with water and surrounding POPC molecules. A, OH group and sn-1 ester oxygen; B, OH group and sn-2 ester oxygen; C, carbonyl oxygen and water; D, OH group and sn-1 carbonyl oxygen; E, OH group and water; F, OH group and phosphate; G, OH group and sn-2 carbonyl oxygen; H, heterocycle oxygen and water.

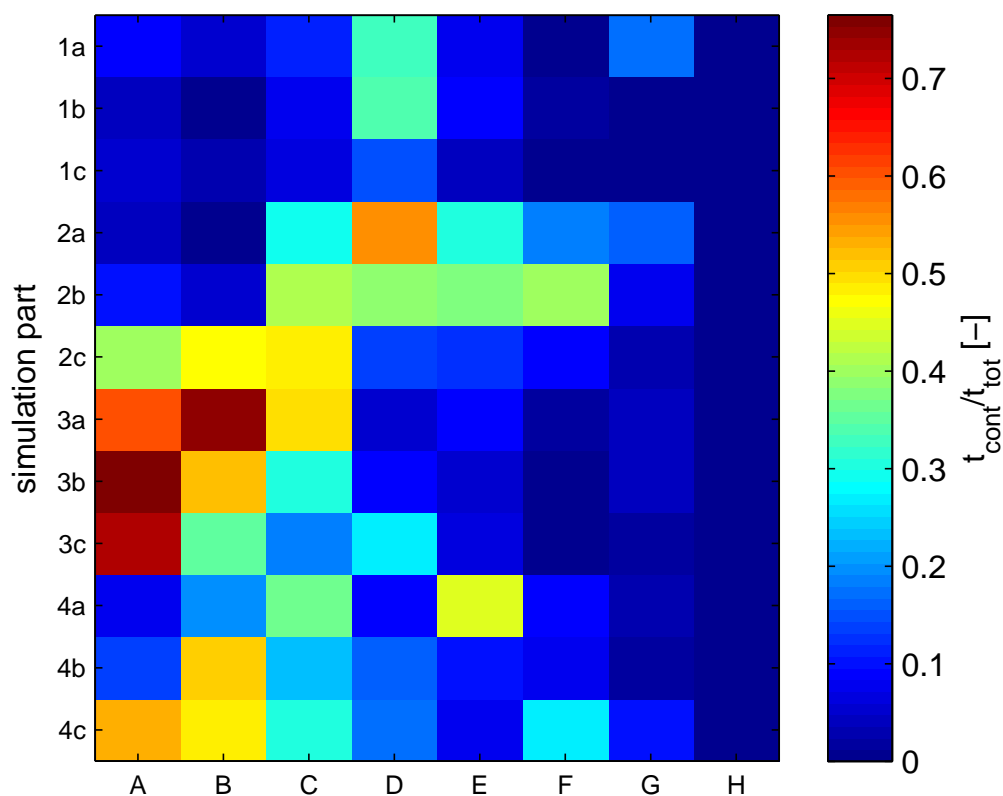


Figure 2.14: Fraction of simulation time spent by selected atoms or groups of the probe in contact with water and surrounding POPC molecules: separate results for twelve 100 ns simulation parts. A, OH group and sn-1 ester oxygen; B, OH group and sn-2 ester oxygen; C, carbonyl oxygen and water; D, OH group and sn-1 carbonyl oxygen; E, OH group and water; F, OH group and phosphate; G, OH group and sn-2 carbonyl oxygen; H, heterocycle oxygen and water.

3. One-Photon Absorption

This chapter deals with 1P TDM calculations. Before the actual calculations for the F2N12S probe are described, a necessary theoretical background is presented, outlining the derivation of the 1P absorption cross section, describing how the 1P TDM can be computed from linear response functions, and introducing time-dependent density functional theory as a powerful method for calculating excited-state properties of medium to large molecules.

3.1 Molecule in an Electromagnetic Field

Let us consider a molecule exposed to an electromagnetic field (Boyd, 2008; Craig and Thirunamachandran, 1984). We denote the wave function describing the state of the molecule by $\Psi(\mathbf{R}_J, \mathbf{r}_j, t)$, where \mathbf{R}_J and \mathbf{r}_j stand for all the nuclear and electronic coordinates of the molecule, respectively. We omit spin coordinates for simplicity. The wave function satisfies the time-dependent Schrödinger equation

$$i\hbar \frac{\partial \Psi(\mathbf{R}_J, \mathbf{r}_j, t)}{\partial t} = \hat{H} \Psi(\mathbf{R}_J, \mathbf{r}_j, t), \quad (3.1)$$

with the Hamiltonian \hat{H} consisting of two components,

$$\hat{H} = \hat{H}_0 + \hat{V}(t). \quad (3.2)$$

The operator \hat{H}_0 is the Hamiltonian of the free molecule, in the absence of the electromagnetic field. The additional term, $\hat{V}(t)$, has a crucial importance, as it describes the interaction of the molecule with the external field,

$$\hat{V}(t) = -\hat{\boldsymbol{\mu}} \cdot \mathbf{E}(t). \quad (3.3)$$

Here, $\hat{\boldsymbol{\mu}}$ is the dipole operator of the molecule,

$$\hat{\boldsymbol{\mu}} = \hat{\boldsymbol{\mu}}^{(n)} + \hat{\boldsymbol{\mu}}^{(e)} = \sum_J q_J \hat{\mathbf{R}}_J - \sum_j e \hat{\mathbf{r}}_j, \quad (3.4)$$

consisting of a nuclear part $\hat{\boldsymbol{\mu}}^{(n)}$ and an electronic part $\hat{\boldsymbol{\mu}}^{(e)}$, and $\mathbf{E}(t)$ is the electric component of the electromagnetic field. For simplicity, we express $\mathbf{E}(t)$ as a monochromatic plane wave. Furthermore, we introduce the dipole approximation, i.e., we neglect the dimensions of the molecule relative to the wavelength of the

electromagnetic radiation. Then $\mathbf{E}(t)$ can be expressed as

$$\mathbf{E}(t) = (Ee^{-i\omega t} + E^*e^{i\omega t}) \mathbf{e}, \quad (3.5)$$

where ω is the frequency of the field, and the vector \mathbf{e} defines the polarization of the electromagnetic wave.

We assume that the solutions $u_n(\mathbf{R}_J, \mathbf{r}_j)$ to the time-independent Schrödinger equation,

$$\hat{H}_0 u_n(\mathbf{R}_J, \mathbf{r}_j) = E_n u_n(\mathbf{R}_J, \mathbf{r}_j), \quad (3.6)$$

for the molecule in the absence of the external field are known. Since these solutions form a complete set, we can express the general solution of the time-dependent Schrödinger equation (3.1) as their linear combination,

$$\Psi(\mathbf{R}_J, \mathbf{r}_j) = \sum_l a_l(t) u_l(\mathbf{R}_J, \mathbf{r}_j) e^{-i\omega_l t}, \quad (3.7)$$

where $\omega_l = E_l/\hbar$. After substituting (3.7) into (3.1), we multiply both sides by $u_m^*(\mathbf{R}_J, \mathbf{r}_j)$, integrate over all nuclear and electronic coordinates, and use the orthonormality of $u_n(\mathbf{R}_J, \mathbf{r}_j)$ to obtain

$$i\hbar \frac{da_m(t)}{dt} = \sum_l a_l(t) V_{ml} e^{-i\omega_{lm}t}. \quad (3.8)$$

Here, ω_{lm} stands for $\omega_{lm} = \omega_l - \omega_m$, and

$$V_{ml} = \int d\mathbf{R}_J d\mathbf{r}_j u_m^*(\mathbf{R}_J, \mathbf{r}_j) \hat{V}(t) u_l(\mathbf{R}_J, \mathbf{r}_j). \quad (3.9)$$

Equation (3.8) is solved by using time-dependent perturbation theory. A parameter λ is inserted into the Hamiltonian

$$\hat{H} = \hat{H}_0 + \lambda \hat{V}(t), \quad (3.10)$$

and the time-dependent coefficients $a_m(t)$ are expressed as a power series in λ ,

$$a_m(t) = a_m^{(0)}(t) + \lambda a_m^{(1)}(t) + \lambda^2 a_m^{(2)}(t) + \dots \quad (3.11)$$

After substituting (3.11) into (3.8) and replacing V_{ml} by λV_{ml} , we compare the terms corresponding to the same power of λ on both sides of (3.8) and thus obtain equations

$$\frac{da_m^{(K)}(t)}{dt} = \frac{1}{i\hbar} \sum_l a_l^{(K-1)} V_{ml} e^{-i\omega_{lm}t}, \quad (3.12)$$

for $K = 1, 2, 3, \dots$

3.2 One-Photon Absorption Cross Section

Equations (3.12) for $K = 1$ are the starting point for the description of 1P absorption (Boyd, 2008; Craig and Thirunamachandran, 1984). We assume that the system is initially in its ground state, denoted by g . At $t = 0$, the electromagnetic field is switched on. Consequently, the coefficients must satisfy

$$a_g^{(0)}(t) = 1, \quad a_l^{(0)}(t) = 0 \quad \text{for } l \neq g \quad (3.13)$$

for all t and

$$a_m^{(K)}(t) = 0 \quad (3.14)$$

for all $t \leq 0$, all m , and all $K > 0$. To calculate the probability of a transition to a state f after the absorption of a single photon, we use equation (3.12) for $K = 1$ and $m = f$. The matrix element V_{fg} can be written as

$$V_{fg} = -(\boldsymbol{\mu}_{fg} \cdot \mathbf{e}) (Ee^{-i\omega t} + E^*e^{i\omega t}), \quad (3.15)$$

where

$$\boldsymbol{\mu}_{fg} = \int d\mathbf{R}_J d\mathbf{r}_j u_f^*(\mathbf{R}_J, \mathbf{r}_j) \hat{\boldsymbol{\mu}} u_g(\mathbf{R}_J, \mathbf{r}_j) \quad (3.16)$$

is the 1P TDM between states g and f . As a consequence, we obtain

$$\frac{da_f^{(1)}(t)}{dt} = -\frac{1}{i\hbar}(\boldsymbol{\mu}_{fg} \cdot \mathbf{e}) (Ee^{i(\omega_{fg}-\omega)t} + E^*e^{i(\omega_{fg}+\omega)t}) \quad (3.17)$$

and after integration

$$a_f^{(1)}(t) = \frac{(\boldsymbol{\mu}_{fg} \cdot \mathbf{e})E}{\hbar(\omega_{fg} - \omega)} [e^{i(\omega_{fg}-\omega)t} - 1] + \frac{(\boldsymbol{\mu}_{fg} \cdot \mathbf{e})E^*}{\hbar(\omega_{fg} + \omega)} [e^{i(\omega_{fg}+\omega)t} - 1]. \quad (3.18)$$

Since we are interested in absorption, we can focus on the former term and omit the latter, which corresponds to the process of stimulated emission bringing the molecule from state f down to g .

The probability that the molecule is in state f at time t is given by

$$p_f^{(1)}(t) = \left| a_f^{(1)}(t) \right|^2 = \frac{|(\boldsymbol{\mu}_{fg} \cdot \mathbf{e})E|^2}{\hbar^2} \left| \frac{e^{i(\omega_{fg}-\omega)t} - 1}{\omega_{fg} - \omega} \right|^2 \quad (3.19)$$

For large t , the probability can be approximated by

$$p_f^{(1)}(t) = \frac{|(\boldsymbol{\mu}_{fg} \cdot \mathbf{e})E|^2}{\hbar^2} 2\pi t \delta(\omega_{fg} - \omega). \quad (3.20)$$

In reality, transitions are subject to various broadening mechanisms, and the infinitely narrow delta function must be replaced by a broader density of final states $\rho_f(\omega_{fg})$. Then the probability is given by

$$p_f^{(1)}(t) = \frac{|(\boldsymbol{\mu}_{fg} \cdot \mathbf{e})E|^2 t}{\hbar^2} \int_0^\infty d\omega_{fg} \rho_f(\omega_{fg}) 2\pi \delta(\omega_{fg} - \omega), \quad (3.21)$$

which is usually written as

$$p_f^{(1)}(t) = \frac{2\pi |(\boldsymbol{\mu}_{fg} \cdot \mathbf{e})E|^2 t}{\hbar^2} \rho_f(\omega_{fg} = \omega). \quad (3.22)$$

The absorption rate can be calculated as

$$R_{fg}^{(1)} = \frac{p_f^{(1)}(t)}{t} = \frac{2\pi |(\boldsymbol{\mu}_{fg} \cdot \mathbf{e})E|^2}{\hbar^2} \rho_f(\omega_{fg} = \omega). \quad (3.23)$$

Comparing (3.23) with (1.1) and using $I = 2\epsilon_0 c |E|^2$, we obtain a formula for the 1P absorption cross section

$$\sigma_{fg}^{(1)} = \frac{\pi}{\hbar^2 \epsilon_0 c} |(\boldsymbol{\mu}_{fg} \cdot \mathbf{e})|^2 \rho_f(\omega_{fg} = \omega). \quad (3.24)$$

We have thus derived a relation between the 1P TDM and the 1P absorption cross section whose consequences we already used in Chapter 1, with the assumption that the 1P TDM is a real vector, for the interpretation of experiments. It remains to be added that if the Born-Oppenheimer approximation is assumed, the wave functions can be factored into a nuclear part $|\phi_m\rangle$ and an electronic part $|\psi_m\rangle$,

$$u_m(\mathbf{R}_J, \mathbf{r}_j) = \phi_m(\mathbf{R}_J) \psi_m(\mathbf{r}_j; \mathbf{R}_J). \quad (3.25)$$

Neglecting the parametric dependence of the electronic wave functions $|\psi_m\rangle$ on the nuclear coordinates \mathbf{R}_J and assuming the orthonormality of $|\psi_m\rangle$, we can

rewrite the 1P TDM as

$$\begin{aligned}
\boldsymbol{\mu}_{fg} &= \int \mathbf{d}\mathbf{R}_J \mathbf{d}\mathbf{r}_j \phi_f^*(\mathbf{R}_J) \psi_f^*(\mathbf{r}_j) \hat{\boldsymbol{\mu}} \phi_g(\mathbf{R}_J) \psi_g(\mathbf{r}_j) \\
&= \int \mathbf{d}\mathbf{R}_J \phi_f^*(\mathbf{R}_J) \phi_g(\mathbf{R}_J) \int \mathbf{d}\mathbf{r}_j \psi_f^*(\mathbf{r}_j) \hat{\boldsymbol{\mu}}^{(e)} \psi_g(\mathbf{r}_j) \\
&\quad + \int \mathbf{d}\mathbf{r}_j \psi_f^*(\mathbf{r}_j) \psi_g^*(\mathbf{r}_j) \int \mathbf{d}\mathbf{R}_J \phi_f^*(\mathbf{R}_J) \hat{\boldsymbol{\mu}}^{(n)} \phi_g^*(\mathbf{R}_J) \\
&= \int \mathbf{d}\mathbf{R}_J \phi_f^*(\mathbf{R}_J) \phi_g(\mathbf{R}_J) \int \mathbf{d}\mathbf{r}_j \psi_f^*(\mathbf{r}_j) \hat{\boldsymbol{\mu}}^{(e)} \psi_g(\mathbf{r}_j),
\end{aligned} \tag{3.26}$$

which, if we neglect the rotational part of $|\phi_m\rangle$, corresponds to the well-known Franck-Condon principle, governing the intensities of vibronic transitions. From (3.26), it follows that in order to determine the direction of the 1P TDM, we only need to evaluate the electronic 1P TDM, which we from now on denote simply as $\boldsymbol{\mu}_{fg}$,

$$\boldsymbol{\mu}_{fg} \equiv \boldsymbol{\mu}_{fg}^{(e)} = \int \mathbf{d}\mathbf{r}_j \psi_f^*(\mathbf{r}_j) \hat{\boldsymbol{\mu}}^{(e)} \psi_g(\mathbf{r}_j). \tag{3.27}$$

In the following section, we show how the elements of the 1P TDM can be obtained from certain linear response functions, and we mention the concepts of time-dependent density functional theory, which we later employ to determine the 1P TDM of the F2N12S probe.

3.3 Linear Response and Time-Dependent Density Functional Theory

Let a molecule in an electronic state $|\psi\rangle$ be exposed to an external perturbation, expressed by $\hat{V}(t)$ in the molecular Hamiltonian (3.2). The operator $\hat{V}(t)$ can be written as

$$\hat{V}(t) = \int_{-\infty}^{\infty} d\omega \hat{V}(\omega) e^{-i\omega t}. \tag{3.28}$$

Suppose that \hat{A} denotes an operator which is time-independent in the Schrödinger picture. Response functions can be used to describe the time development of the

mean value of \hat{A} as (Salek et al., 2002)

$$\begin{aligned}
\langle \hat{A} \rangle(t) &= \langle \psi(0) | \hat{A} | \psi(0) \rangle + \int_{-\infty}^{\infty} d\omega_1 e^{-i\omega_1 t} \langle \langle \hat{A}; \hat{V}(\omega_1) \rangle \rangle_{\omega_1} + \\
&+ \int_{-\infty}^{\infty} d\omega_1 \int_{-\infty}^{\infty} d\omega_2 e^{(-i\omega_1 - i\omega_2)t} \langle \langle \hat{A}; \hat{V}(\omega_1), \hat{V}(\omega_2) \rangle \rangle_{\omega_1, \omega_2} + \\
&+ \int_{-\infty}^{\infty} d\omega_1 \int_{-\infty}^{\infty} d\omega_2 \int_{-\infty}^{\infty} d\omega_3 e^{(-i\omega_1 - i\omega_2 - i\omega_3)t} \langle \langle \hat{A}; \hat{V}(\omega_1), \hat{V}(\omega_2), \hat{V}(\omega_3) \rangle \rangle_{\omega_1, \omega_2, \omega_3} \\
&+ \dots
\end{aligned} \tag{3.29}$$

Here, the terms

$$\langle \langle \hat{A}; \hat{V}(\omega_1) \rangle \rangle_{\omega_1} \tag{3.30}$$

$$\langle \langle \hat{A}; \hat{V}(\omega_1), \hat{V}(\omega_2) \rangle \rangle_{\omega_1, \omega_2} \tag{3.31}$$

$$\langle \langle \hat{A}; \hat{V}(\omega_1), \hat{V}(\omega_2), \hat{V}(\omega_3) \rangle \rangle_{\omega_1, \omega_2, \omega_3} \tag{3.32}$$

are the linear, quadratic, and cubic frequency-dependent response functions, respectively.

The important thing is the fact that linear response functions can be used to determine the components of the 1P TDM, even without an explicit knowledge of the excited-state wave function. Assuming that the molecule interacts with a monochromatic plane wave (3.5), the components $(\mu_{fg})_j$ of the electronic 1P TDM between states g and f can be calculated from residues of the linear response functions $\langle \langle \hat{\mu}_j; \hat{\mu}_j \rangle \rangle_{\omega}$ (Olsen and Jorgensen, 1985), since

$$\lim_{\omega \rightarrow \omega_{fg}} (\omega - \omega_{fg}) \langle \langle \hat{\mu}_j; \hat{\mu}_j \rangle \rangle_{\omega} = |(\mu_{fg})_j|^2. \tag{3.33}$$

The expressions (3.33) can be evaluated using time-dependent density functional theory (TD-DFT). TD-DFT is a powerful method employed to determine excitation energies, transition moments, and excited-state properties for medium-sized to large molecules (Dreuw and Head-Gordon, 2005). Similarly to the classical ground-state density functional theory (DFT), an introduction to which can be found, e.g., in (Cramer, 2002), TD-DFT replaces the multidimensional electronic wavefunction $|\psi\rangle$ with a three-dimensional one-particle density function

$$n(\mathbf{r}, t) = \int d^3\mathbf{r}_2 \dots \int d^3\mathbf{r}_N \psi^*(\mathbf{r}, \mathbf{r}_2, \dots, \mathbf{r}_N, t) \psi(\mathbf{r}, \mathbf{r}_2, \dots, \mathbf{r}_N, t), \tag{3.34}$$

now assumed to be time-dependent. The Runge-Gross theorem (Marques et al., 2012) guarantees that there exists a one-to-one mapping between the one-particle

density $n(\mathbf{r}, t)$ and a time-dependent one-particle external potential

$$\hat{V}_{ext}(\mathbf{r}_1, \mathbf{r}_2, \dots, \mathbf{r}_N, t) = \sum_{l=1}^N \hat{v}_{ext}(\mathbf{r}_l, t). \quad (3.35)$$

The Runge-Gross theorem implies that describing the time development of a system by means of the simple one-particle density is equivalent to using the full wave function.

The one-particle density is calculated from N Kohn-Sham orbitals $\varphi_l(\mathbf{r}, t)$ as

$$n(\mathbf{r}, t) = \sum_{l=1}^N |\varphi_l(\mathbf{r}, t)|^2. \quad (3.36)$$

The Kohn-Sham orbitals satisfy the time-dependent Kohn-Sham equations (Marques et al., 2012) (in atomic units),

$$i \frac{\partial}{\partial t} \varphi_j(\mathbf{r}, t) = \left[-\frac{\nabla^2}{2} + \hat{v}_{KS}(\mathbf{r}, t) \right] \varphi_j(\mathbf{r}, t), \quad (3.37)$$

where \hat{v}_{KS} is the Kohn-Sham operator defined as

$$\hat{v}_{KS} = \hat{v}_{ext}(\mathbf{r}, t) + \int d^3 \mathbf{r}' \frac{n(\mathbf{r}', t)}{|\mathbf{r} - \mathbf{r}'|} + \hat{v}_{xc}(\mathbf{r}, t). \quad (3.38)$$

The second and the third term in (3.38) are both functionals of the density $n(\mathbf{r}, t)$. The latter term is the exchange-correlation potential

$$\hat{v}_{xc}(\mathbf{r}, t) = \frac{\delta E_{xc}}{\delta n(\mathbf{r})} \Big|_{n(\mathbf{r})=n(\mathbf{r}, t)}, \quad (3.39)$$

derived from the exchange-correlation functional E_{xc} , which plays an essential role in TD-DFT calculations. The exact exchange-correlation functional E_{xc} is not known; therefore, approximate functionals must be employed. There are a number of approximate exchange-correlation functionals. These include local functionals, gradient-corrected functionals, and hybrid functionals (Dreuw and Head-Gordon, 2005). As described in detail, e.g., in (Salek et al., 2002), the Kohn-Sham orbitals and the Kohn-Sham equations (3.37) can be used to formulate equations whose solution gives a general linear response function $\langle\langle A; \hat{V}(\omega) \rangle\rangle_\omega$. On the basis of (3.33), TD-DFT then allows for a calculation of the 1P TDM.

3.4 One-Photon Transition Dipole Moment of F2N12S

In order to be able to reconstruct the orientational distribution of the 1P TDM from MD simulations, we needed to know how the 1P TDM is oriented relative to the molecular geometry of the F2N12S probe embedded in the POPC bilayer and, furthermore, how stable the orientation is with respect to changes in the membrane environment and in the conformation of the fluorescent probe.

To gain information on the direction of the 1P TDM relative to the molecular frame and on the stability of that direction, we extracted a series of geometries from the four MD trajectories described in Chapter 2, after the probe stabilized in the bilayer, and calculated the 1P TDM corresponding to the $S_0 \mapsto S_1$ transition for each of them. We used the TD-DFT implementation in Gaussian 09, employing the hybrid B3LYP functional with the def2-SVP basis set (Schafer et al., 1992). Inspired by the work of (Cwiklik et al., 2011) on the PRODAN probe, we modeled the surrounding lipid and water environment as electrostatic point charges. To lower the computational cost of the 1P TDM calculations, the nine CH_n groups of the twelve-carbon alkyl chain of the probe most distant from the aromatic rings were not included into the quantum mechanical system. Hydrogen atoms were added to the united-atom geometries of the probe using the Open Babel package (O’Boyle et al., 2011). The calculated directions of the 1P TDM relative to the geometries of the probe were described in terms of two angles, γ and δ , the former between the projection of the 1P TDM onto the plane of the aromatic ring containing atoms CAN and CAI (see Figure 2.6) and the vector connecting these two atoms, the latter indicating the deviation of the 1P TDM from the plane of the aromatic ring.

To justify the choice of the functional and basis set, we performed several benchmarks. We compared the hybrid B3LYP functional with its long-range corrected version CAM-B3LYP (Yanai et al., 2004), which should more accurately describe excitations involving long-range charge transfer (Dreuw and Head-Gordon, 2005). The results yielded by these two functionals for an optimized geometry in vacuum are shown in Table 3.1. We found that the 1P TDM directions differed not too significantly by 3.4° between the functionals. We went on to calculate the electronic excitation wavelengths using the two functionals for a series of ten geometries taken from the MD simulations and compared the results with the absorption spectrum reported by the manufacturer (Figure 3.1), peaking at ~ 420 nm. With an average value of 433 nm, the wavelengths obtained using B3LYP were significantly closer to the peak in the experimental absorption spectrum than those calculated using CAM-B3LYP (average 364 nm). Therefore,

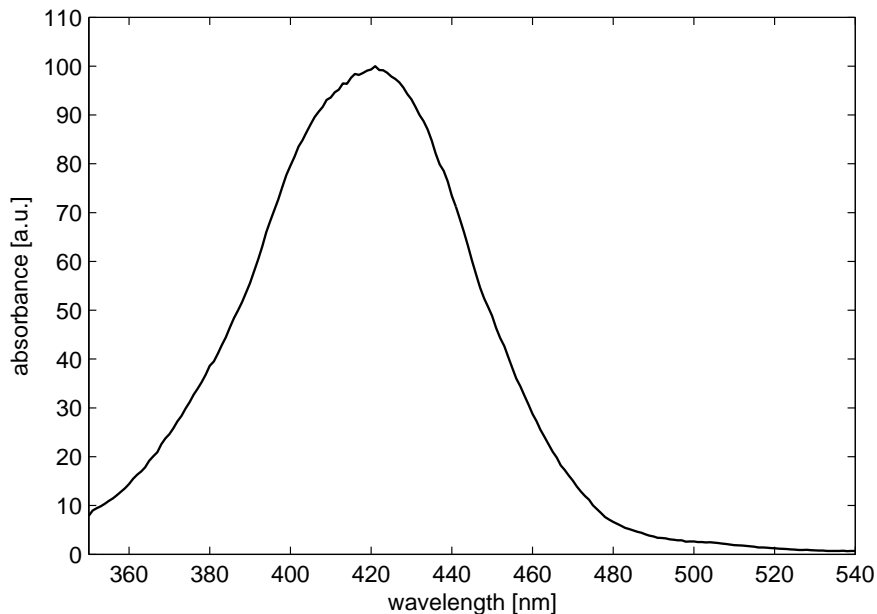


Figure 3.1: Absorption spectrum of the F2N12S probe embedded in a lipid bilayer as reported by the manufacturer (Life Technologies, accessed April 2, 2013).

we chose the B3LYP functional for our further calculations. Moreover, we investigated the effect of the basis set on the direction of the 1P TDM. As can be seen in Table 3.2, the choice of the basis set had little influence on the direction of the 1P TDM.

In total, we randomly selected 87 geometries from the four MD trajectories. Despite the differences in geometry and the effects of the environment, the direction of the 1P TDM expressed by the angles γ and δ proved to be constant within a few degrees. The average values of γ and δ equaled $\gamma = 9.1^\circ$ and $\delta = 1.1^\circ$, with their standard deviations being 2.2° and 5.2° , respectively. The average direction of the 1P TDM is depicted in Figure 3.2. The relative stability of the 1P TDM direction with respect to the molecular frame allowed us to calculate the orientational distribution of the 1P TDM in the bilayer by taking the direction of the 1P TDM with respect to the molecule as fixed and equal to the average direction obtained from the series of 87 geometries.

functional/basis set	γ [$^\circ$]	δ [$^\circ$]
B3LYP/def2-SVP	9.27	-1.82
CAM-B3LYP/def2-SVP	12.63	-1.65

Table 3.1: Comparison of the 1P TDM directions yielded by B3LYP and CAM-B3LYP for a B3LYP/cc-pVDZ optimized geometry in vacuum.

functional/basis set	γ [°]	δ [°]
B3LYP/def2-SVP	9.27	-1.82
B3LYP/6-31G	9.27	-1.76
B3LYP/cc-pVDZ	9.18	-1.89
B3LYP/cc-pVTZ	9.11	-1.93

Table 3.2: Dependence of the 1P TDM direction on the choice of basis set for a B3LYP/cc-pVDZ optimized geometry in vacuum.

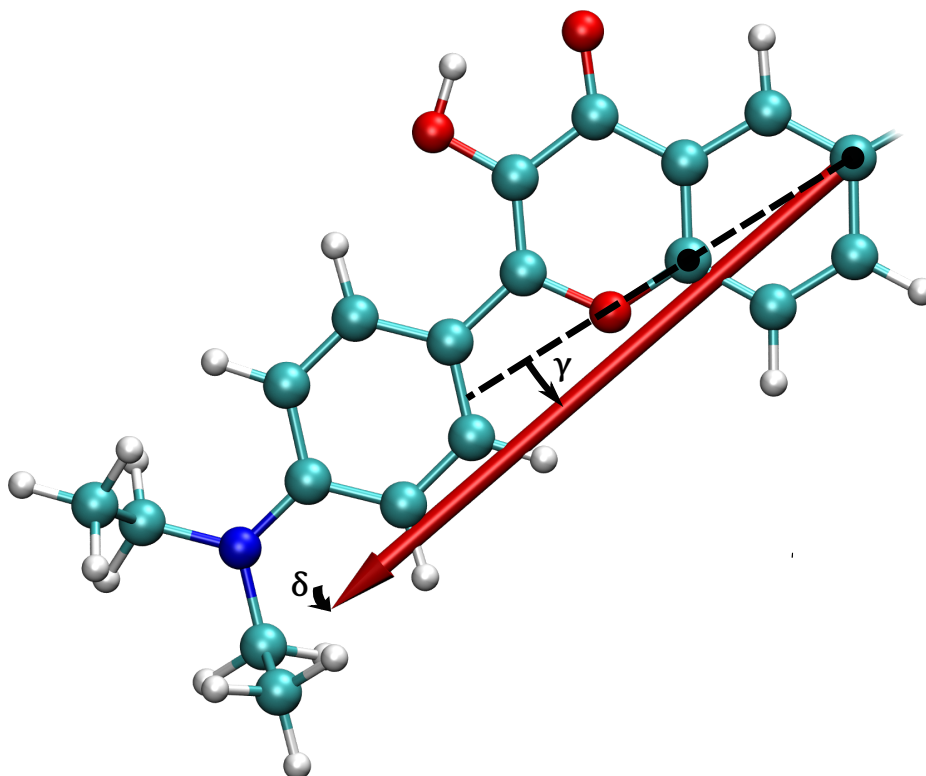


Figure 3.2: Average direction of the 1P TDM with respect to the aromatic rings of the F2N12S probe. $\gamma = 9.1^\circ$ is the angle between the axis defined by the two marked atoms and the projection of the 1P TDM onto the plane of the aromatic ring shared by the marked atoms; $\delta = 1.1^\circ$ quantifies the deviation of the 1P TDM from the plane of the aromatic ring.

4. Two-Photon Absorption

In this chapter, we start with the theory behind 2P absorption. Our primary goal is to characterize conditions which allow simplifying the description of 2P absorption anisotropy by replacing the general 2P transition tensor by a much simpler vector corresponding to the 1P TDM between the ground and final states. By performing calculations of its 2P absorption properties, we examine whether these conditions are met by the F2N12S probe.

4.1 Two-Photon Absorption Cross Section

To derive a formula for the 2P absorption cross section, similarly to the case of 1P absorption, we start with equations (3.12) for coefficients $a_m^{(K)}(t)$, this time considering $K = 2$. We make use of the solutions (3.18) that we have already found for $a_l^{(1)}(t)$. Substituting (3.18) into (3.12) and omitting all terms that are not related to 2P absorption, we obtain a differential equation (Boyd, 2008)

$$\frac{da_f^{(2)}(t)}{dt} = -\frac{1}{i\hbar} \sum_m \frac{(\boldsymbol{\mu}_{fm} \cdot \mathbf{e})(\boldsymbol{\mu}_{mg} \cdot \mathbf{e})E^2}{\hbar(\omega_{mg} - \omega)} e^{i(\omega_{fg} - 2\omega)t}. \quad (4.1)$$

After its integration, we get

$$a_f^{(2)}(t) = \sum_m \frac{(\boldsymbol{\mu}_{fm} \cdot \mathbf{e})(\boldsymbol{\mu}_{mg} \cdot \mathbf{e})E^2}{\hbar^2(\omega_{mg} - \omega)} \frac{e^{i(\omega_{fg} - 2\omega)t} - 1}{\omega_{fg} - 2\omega}. \quad (4.2)$$

Analogously to 1P absorption, we can compute the probability of 2P absorption as

$$p_f^{(2)}(t) = \left| a_f^{(2)}(t) \right|^2 = \left| \sum_m \frac{(\boldsymbol{\mu}_{fm} \cdot \mathbf{e})(\boldsymbol{\mu}_{mg} \cdot \mathbf{e})E^2}{\hbar^2(\omega_{mg} - \omega)} \right|^2 \left| \frac{e^{i(\omega_{fg} - 2\omega)t} - 1}{\omega_{fg} - 2\omega} \right|^2, \quad (4.3)$$

which for high t becomes

$$p_f^{(2)}(t) = \left| \sum_m \frac{(\boldsymbol{\mu}_{fm} \cdot \mathbf{e})(\boldsymbol{\mu}_{mg} \cdot \mathbf{e})E^2}{\hbar^2(\omega_{mg} - \omega)} \right|^2 2\pi t \delta(\omega_{fg} - 2\omega), \quad (4.4)$$

or, taking into account line broadening,

$$p_f^{(2)}(t) = \left| \sum_m \frac{(\boldsymbol{\mu}_{fm} \cdot \mathbf{e})(\boldsymbol{\mu}_{mg} \cdot \mathbf{e})E^2}{\hbar^2(\omega_{mg} - \omega)} \right|^2 2\pi t \rho_f(\omega_{fg} = 2\omega). \quad (4.5)$$

The 2P absorption rate then equals

$$R_{fg}^{(2)} = \left| \sum_m \frac{(\boldsymbol{\mu}_{fm} \cdot \mathbf{e})(\boldsymbol{\mu}_{mg} \cdot \mathbf{e})E^2}{\hbar^2(\omega_{mg} - \omega)} \right|^2 2\pi \rho_f(\omega_{fg} = 2\omega). \quad (4.6)$$

If we compare (4.6) with (1.2) and express the intensity of the electromagnetic radiation as $I = 2\epsilon_0 c |E|^2$, we obtain the following formula for the 2P absorption cross section:

$$\sigma_{fg}^{(2)} = \frac{1}{2\epsilon_0^2 \hbar^4 c^2} \left| \sum_m \frac{(\boldsymbol{\mu}_{fm} \cdot \mathbf{e})(\boldsymbol{\mu}_{mg} \cdot \mathbf{e})}{(\omega_{mg} - \omega)} \right|^2 2\pi \rho_f(\omega_{fg} = 2\omega). \quad (4.7)$$

The sum in the absolute value can be written as

$$\sum_m \frac{(\boldsymbol{\mu}_{fm} \cdot \mathbf{e})(\boldsymbol{\mu}_{mg} \cdot \mathbf{e})}{(\omega_{mg} - \omega)} = \frac{1}{2} \mathbf{e}^T \mathbf{S}_{fg} \mathbf{e}, \quad (4.8)$$

where \mathbf{S}_{fg} is the 2P transition tensor with elements

$$(\mathbf{S}_{fg})_{kl} = \sum_m \left[\frac{(\mu_{fm})_k (\mu_{mg})_l}{(\omega_{mg} - \omega)} + \frac{(\mu_{fm})_l (\mu_{mg})_k}{(\omega_{mg} - \omega)} \right]. \quad (4.9)$$

The elements of the 2P electronic transition tensor \mathbf{S}_{fg} can be determined using TD-DFT based on the formalism of response theory, introduced in Chapter 3. More specifically, they can be calculated from residues of the quadratic response functions $\langle\langle \hat{\mu}_j; \hat{\mu}_k, \hat{\mu}_l \rangle\rangle_{\omega_{fg}/2, \omega}$, since (Frediani et al., 2005; Salek et al., 2003; Olsen and Jorgensen, 1985)

$$\lim_{\omega \rightarrow \omega_{fg}} (\omega - \omega_{fg}) \langle\langle \hat{\mu}_j; \hat{\mu}_k, \hat{\mu}_l \rangle\rangle_{\omega_{fg}/2, \omega} = -(\mathbf{S}_{fg})_{jk} (\mu_{fg})_l. \quad (4.10)$$

4.2 Approximation of a Two-Photon Transition Tensor by a One-Photon Transition Dipole Moment

The 2P transition tensor \mathbf{S}_{fg} is symmetric. If its elements are real, it can be diagonalized. Suppose that it has a single dominant eigenvalue, with the other two eigenvalues being close to zero. Then the 2P absorption cross section is maximal if the electric field vector is aligned with the eigenvector corresponding to the dominant eigenvalue, and it decays with \cos^4 of the angle between the two vectors. In the following, we describe a particular case with the eigenvector being almost identical to the 1P TDM.

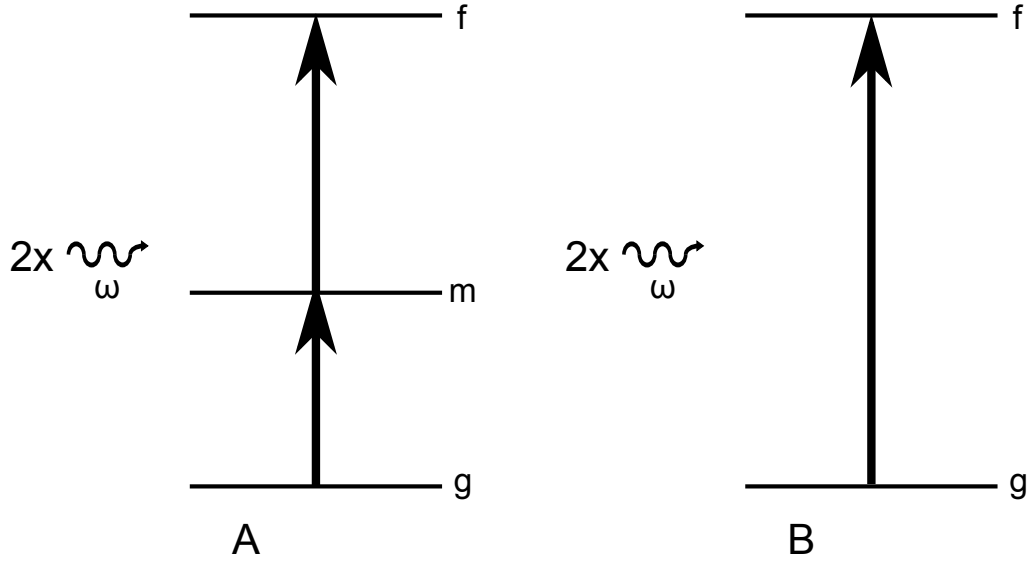


Figure 4.1: 2P transition via an intermediate state (A) and directly to the final excited state (B).

Let us look again at the sum in (4.8). The index m runs over all states of the molecule, including the ground state g and the final state f . Therefore, the sum can be rewritten as

$$\begin{aligned} \sum_m \frac{(\boldsymbol{\mu}_{fm} \cdot \mathbf{e})(\boldsymbol{\mu}_{mg} \cdot \mathbf{e})}{(\omega_{mg} - \omega)} &= \sum_{m \neq g, f} \frac{(\boldsymbol{\mu}_{fm} \cdot \mathbf{e})(\boldsymbol{\mu}_{mg} \cdot \mathbf{e})}{(\omega_{mg} - \omega)} + \\ &+ \frac{(\boldsymbol{\mu}_{fg} \cdot \mathbf{e})(\boldsymbol{\mu}_{gg} \cdot \mathbf{e})}{(-\omega)} + \frac{(\boldsymbol{\mu}_{ff} \cdot \mathbf{e})(\boldsymbol{\mu}_{fg} \cdot \mathbf{e})}{(\omega_{fg} - \omega)}. \end{aligned} \quad (4.11)$$

Here, $\boldsymbol{\mu}_{gg}$ and $\boldsymbol{\mu}_{ff}$ denote the electric dipole moments of the ground and final excited state, respectively. Assuming that the electromagnetic field is tuned at half the frequency of the $g \mapsto f$ transition, i.e., $\omega = \omega_{fg}/2$, we can rewrite (4.11) as (Drobizhev et al., 2006; Karotki, 2003)

$$\sum_m \frac{(\boldsymbol{\mu}_{fm} \cdot \mathbf{e})(\boldsymbol{\mu}_{mg} \cdot \mathbf{e})}{(\omega_{mg} - \omega)} = \sum_{m \neq g, f} \left[\frac{(\boldsymbol{\mu}_{fm} \cdot \mathbf{e})(\boldsymbol{\mu}_{mg} \cdot \mathbf{e})}{(\omega_{mg} - \omega)} \right] + \frac{1}{\omega} (\boldsymbol{\mu}_{fg} \cdot \mathbf{e})(\Delta \boldsymbol{\mu}_{fg} \cdot \mathbf{e}), \quad (4.12)$$

where $\boldsymbol{\mu}_{fg}$ is the 1P TDM between states g and f , and $\Delta \boldsymbol{\mu}_{fg} = \boldsymbol{\mu}_{ff} - \boldsymbol{\mu}_{gg}$ denotes the change in the electric dipole moment of the molecule caused by the transition between g and f . The sum on the rhs of (4.12) describes the process of 2P absorption as if proceeding via all possible intermediate excited states m (Figure 4.1A). On the other hand, the second term on the rhs of (4.12) corresponds to

a direct transition between the ground state and the final excited state (Figure 4.1B).

Let us assume that we can neglect the contribution of the transitions via intermediate states. Then the 2P absorption cross section is determined exclusively by the second term on the rhs of (4.12), and we can write

$$\sigma_{fg}^{(2)} \propto |(\boldsymbol{\mu}_{fg} \cdot \mathbf{e})(\Delta\boldsymbol{\mu}_{fg} \cdot \mathbf{e})|^2 \quad (4.13)$$

Moreover, let us suppose that the 1P TDM $\boldsymbol{\mu}_{fg}$ is real and parallel to the vector $\Delta\boldsymbol{\mu}_{fg}$, which describes the change in the electric dipole moment between states g and f . Then (4.13) can be rewritten as

$$\sigma_{fg}^{(2)} \propto (\boldsymbol{\mu}_{fg} \cdot \mathbf{e})^4, \quad (4.14)$$

and the 2P absorption cross section becomes proportional to \cos^4 of the angle between the 1P TDM and the electric field vector, which justifies the relation (1.4) used in Chapter 1.

It follows from the above considerations that we can use the 1P TDM to describe 2P absorption anisotropy provided two conditions are satisfied. First, the term containing the 1P TDM and the change in the electric dipole moment must be large compared to the sum over all the intermediate states in (4.12). This happens if the frequency ω of the electromagnetic radiation is not close to any of the excitation frequencies ω_{mg} , and if the change $\Delta\boldsymbol{\mu}_{fg}$ in the electric dipole moment is sufficiently large. Second, the 1P TDM $\boldsymbol{\mu}_{fg}$ between the ground state and the final excited state must be approximately parallel to $\Delta\boldsymbol{\mu}_{fg}$. Fluorescent probes satisfying these conditions are particularly useful for LD measurements, as they allow for a much simpler interpretation of experimental data than fluorescent probes possessing a general 2P transition tensor.

4.3 Two-Photon Absorption of F2N12S

To test whether the 2P transition tensor between states S_0 and S_1 of the F2N12S probe has a single dominant eigenvalue, and whether the corresponding eigenvector is aligned with the 1P TDM, we performed a calculation of the 2P transition tensor in vacuum for the B3LYP/cc-pVDZ optimized geometry with the truncated alkyl chain, used in Chapter 2 for parametrization of the MD model. We used quadratic response TD-DFT as implemented in the DALTON program (Angeli et al., 2011) and employed the B3LYP functional with the cc-pVDZ basis set.

Having obtained the 2P transition tensor, we diagonalized it and confirmed

that it had a single dominant eigenvalue, as documented in Table 4.1. Since the absorption cross sections along the eigenvectors of the tensor depend on the squares of the corresponding eigenvalues, it follows from Table 4.1 that the absorption cross sections in directions perpendicular to the eigenvector corresponding to the dominant eigenvalue form less than 0.03 % of the dominant contribution. Therefore, their influence can safely be neglected, and the 2P absorption anisotropy is effectively determined by the eigenvector corresponding to the dominant eigenvalue.

λ_1	λ_2	λ_3
-422.9	6.6	0.3

Table 4.1: Eigenvalues of the 2P transition tensor between states S_0 and S_1 of the F2N12S probe (in atomic units).

Using the same functional and basis set in DALTON, we went on to calculate the direction of the change $\Delta\boldsymbol{\mu}_{fg}$ in the electric dipole moment. In Figure 4.2, the directions of $\Delta\boldsymbol{\mu}_{fg}$ and the eigenvector \boldsymbol{v}_1 corresponding to the dominant eigenvalue are compared to that of the 1P TDM. We found that the angle between $\Delta\boldsymbol{\mu}_{fg}$ and the direction parallel to the 1P TDM was 8.9° . The eigenvector \boldsymbol{v}_1 differed in its orientation from the 1P TDM by 5.0° .

Further effort is needed to test the present TD-DFT calculations of the 2P transition tensor against more expensive high-accuracy methods, such as the equation-of-motion coupled cluster, and to investigate the effects of the membrane environment. Nevertheless, the present results already show a clear "vector-like" behavior of the 2P transition tensor and indicate that the 2P absorption anisotropy of the F2N12S probe can at least approximately be described by the 1P TDM.

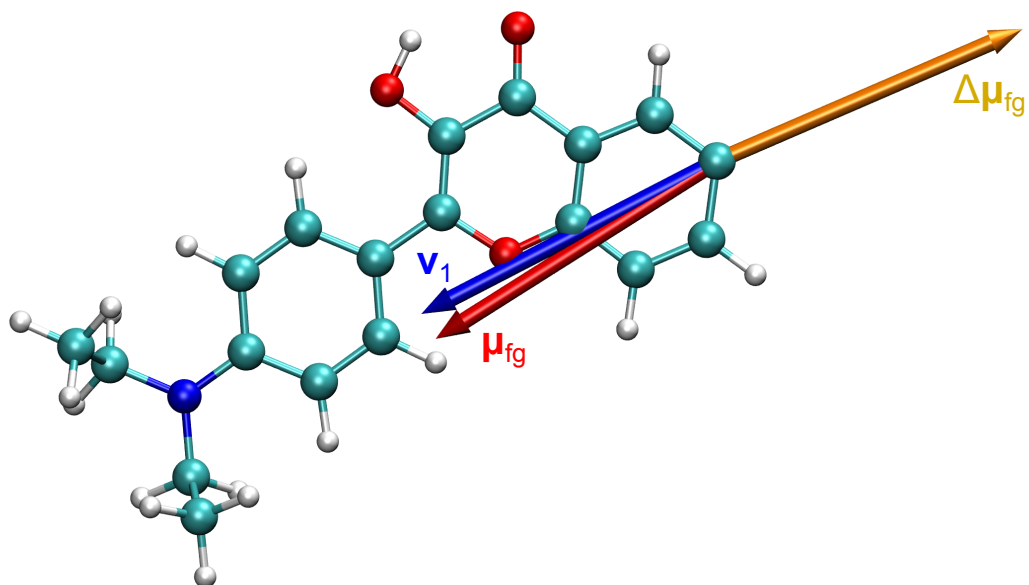


Figure 4.2: Directions of $\Delta\mu_{fg}$, the change in the electric dipole moment, v_1 , the eigenvector corresponding to the dominant eigenvalue of the 2P transition tensor, and μ_{fg} , the 1P TDM, relative to the aromatic rings of the F2N12S probe.

5. Orientational Distribution

Having performed MD simulations of the F2N12S probe in a POPC membrane and quantum calculations of the probe’s absorption properties, we are now ready to predict the orientational distribution of the 1P TDM from simulations and compare the prediction with estimates based on experiments. We also check how the different experimental estimates stand the comparison with the result of computer modeling. In addition, we discuss the level of convergence of the orientational distribution acquired from simulations.

5.1 Simulations vs Experiments

The orientational distribution of the 1P TDM in the membrane, i.e., the histogram of the angle α between the 1P TDM and the membrane normal, could easily be acquired from MD trajectories, since, as we demonstrated in Chapter 3, we could take the direction of the 1P TDM relative to the molecular geometry of the F2N12S probe as fixed. The overall orientational distribution of the 1P TDM, obtained by combining data from four independent trajectories, is shown in Figure 5.1. The distribution exhibits a single peak and is relatively broad, which reflects the liquid disordered phase state of the POPC membrane. The mean value and the standard deviation of the distribution are 47.9° and 13.3° , respectively.

We can now compare the result of MD with experimental estimates of the orientational distribution. Figures 5.2–5.4 show estimates based on the Gaussian function (1.18), the first three terms (1.27) of the Legendre expansion, and the entropy-maximizing function (1.31) confronted with the orientational distribution obtained from MD. We note that in all three cases, the peaks of the experimental estimates are shifted by only several degrees towards higher values of α compared to MD results. There is thus an almost quantitative agreement between the experimental estimates and the orientational distribution obtained from MD in that each of the distributions is formed by a single peak of a comparable width located in the middle region of α . To make the comparisons even more quantitative, Table 5.1 contains the means and standard deviations of the distributions (with the exception of the estimate based on the first three terms of the Legendre expansions, which assumes negative values, and for which the calculation of the mean or standard deviation would, evidently, not make sense). The table reveals less than a 6° shift in the mean values of the experimental estimates relative to the mean of the MD result. At the same time, the experimental standard deviations

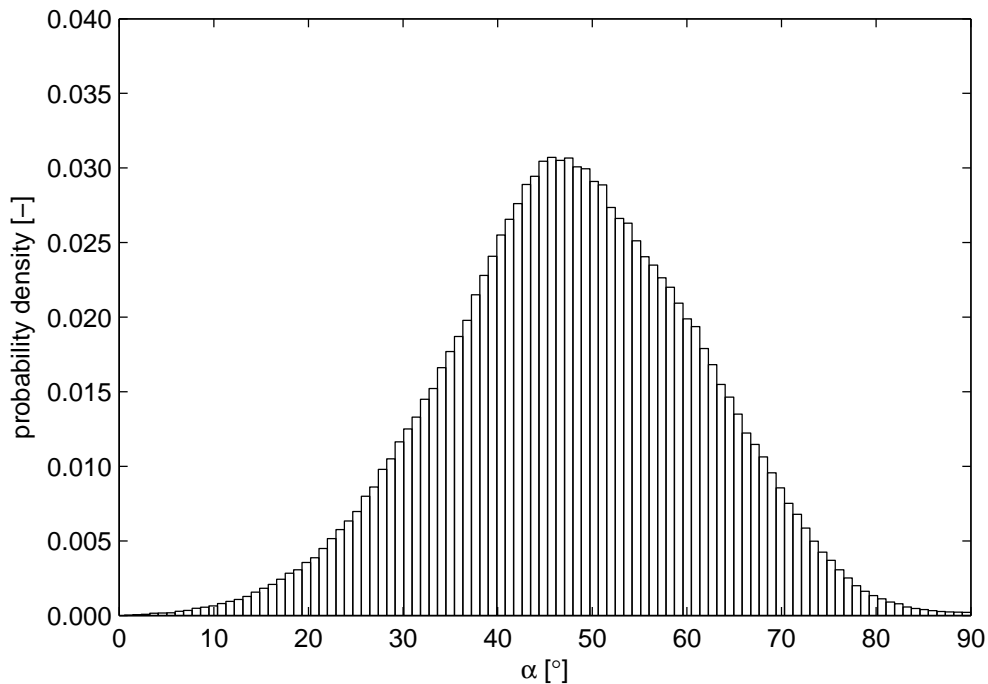


Figure 5.1: Orientational distribution of the 1P TDM of the F2N12S probe in a POPC bilayer, i.e. the distribution of the angle α between the 1P TDM and the membrane normal, obtained from MD simulations.

are close to the result of MD, which is especially true for the Gaussian function. In comparison, the entropy-maximizing distribution, with its more pronounced tail in the region of high α , is optimized to be the broadest of all distributions under the constraints given by experiments; therefore, its standard deviation can be regarded as an upper limit for the standard deviation of the real orientational distribution. The slight shift in the mean values between MD and experiments may be blamed on an imperfect force field and, in part, also on a possibility of having a not fully converged distribution, as discussed in the following section. Other factors contributing to the shift may include the presence of noise in the experimental data or an imperfect polarization of the excitation light in the focal region, which may occur in the case of 1P absorption. These factors would decrease LD and thus move the estimated mean value of the orientational distribution towards the angles of 54.7° or 52.0° , characterized by vanishing 1P and 2P LD, respectively.

The orientational distribution acquired using MD resembles a Gaussian-shaped function. To confirm its Gaussian character, we tried to fit the orientational distribution obtained from MD with a Gaussian-based distribution function. The result is presented in Figure 5.5. It proves that the orientational distribution gained from MD can be accurately described as a Gaussian-based distribution characterized by parameters $\alpha_0 = 44.7^\circ$ and $\sigma = 14.3^\circ$, thus differing by 5.5° in

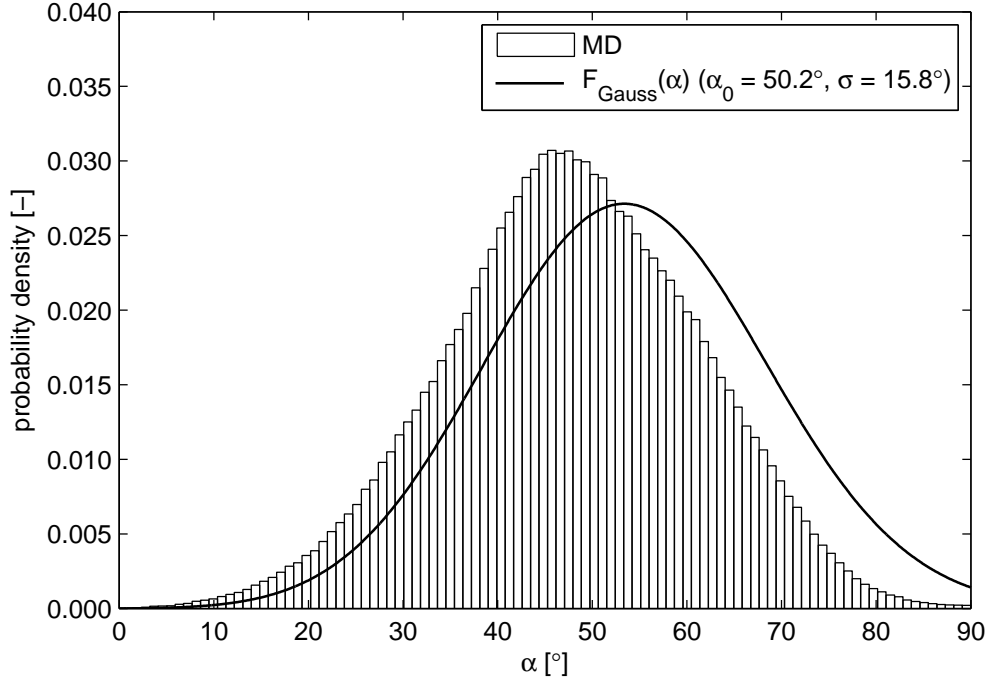


Figure 5.2: Orientational distribution obtained from MD compared with a Gaussian-based experimental estimate.

α_0 and by only 1.5° in σ from the Gaussian-based experimental estimate. This observation indicates that it is reasonable to assume a Gaussian character of the orientational distribution when interpreting LD measurements with fluorescent probes embedded in membranes in the liquid disordered phase, where the probes are not too restricted in their motions by the surrounding environment and are thus likely to exhibit a relatively broad, continuous distribution of tilts rather than to be held in a single or several distinct, well-separated orientations.

	mean [°]	standard deviation [°]
MD total	47.9	13.3
$F_{Gauss}(\alpha)$	53.4 ± 0.1	14.3 ± 0.5
$F_S(\alpha)$	53.7 ± 0.1	14.7 ± 0.5

Table 5.1: Comparison of means and standard deviations of orientational distributions obtained from MD simulations and experiments. $F_{Gauss}(\alpha)$ denotes the Gaussian-based estimate and $F_S(\alpha)$ the entropy-maximizing distribution.

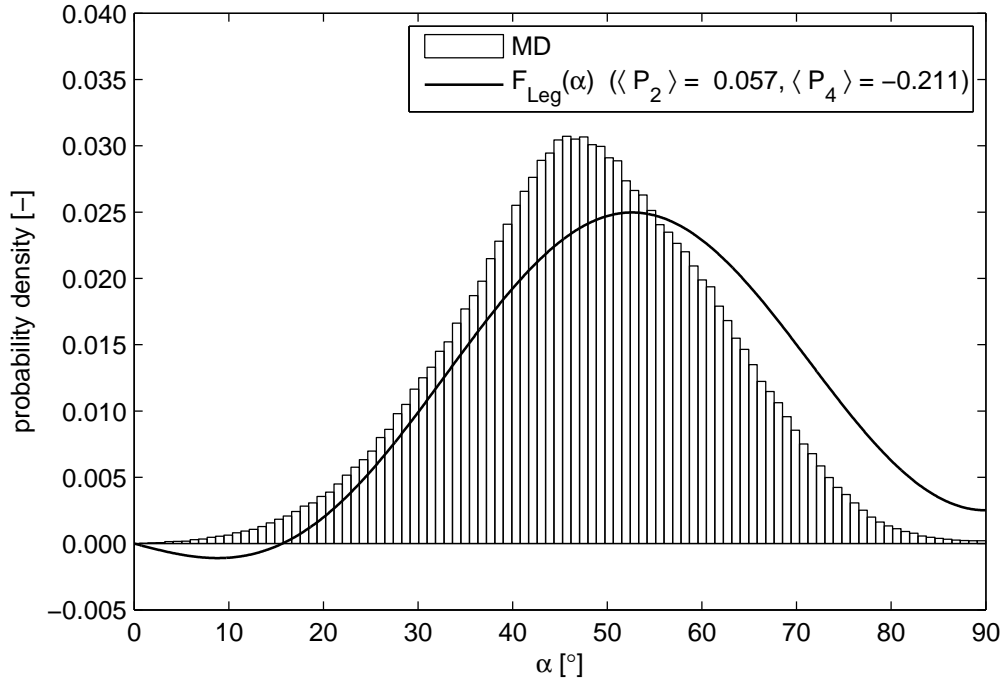


Figure 5.3: Orientational distribution obtained from MD compared with an experimental estimate based on the first three terms of the Legendre expansion.

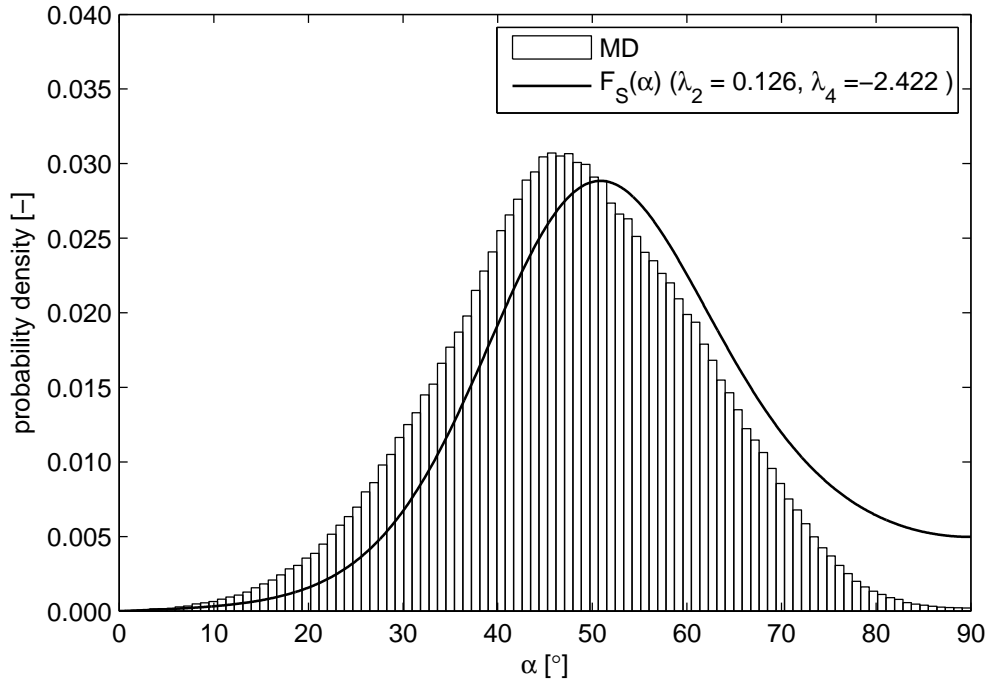


Figure 5.4: Orientational distribution obtained from MD compared with an entropy-maximizing experimental estimate.

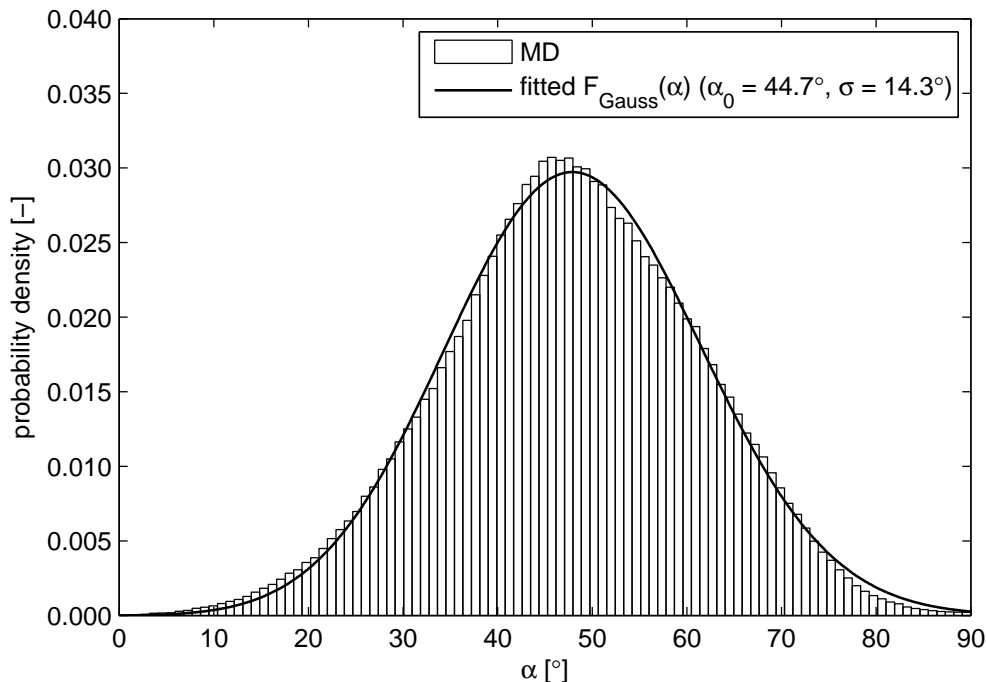


Figure 5.5: Orientational distribution obtained from MD fitted with a Gaussian-based distribution function.

5.2 Convergence of Orientational Distributions Obtained from Simulations

In the previous section, we presented results of MD simulations obtained by combining four independent trajectories, each of them sampling a certain part of the configuration space of the fluorescent probe embedded in the membrane. In an ideal case, each trajectory would sample the complete configuration space, and the orientational distributions gained from the individual simulations would be identical to the overall result. As it is shown in Figure 5.6, our sampling time was not sufficient to achieve such a perfectly converged situation. While the individual distributions exhibit a large overlap between each other and give a good idea about the character of the orientational distribution, differences remain in the details of the shapes of the distributions and the exact positions of their peaks. This is further illustrated by Table 5.2, containing the means and standard deviations of the individual distributions, and by Figure 5.7, which shows the average values of means and standard deviations from MD trajectories and their 95% confidence intervals in comparison with experimental findings. A substantial prolongation of the sampling time would be required to reach full convergence. However, simulation times spanning several microseconds are not yet readily achievable in conventional atomistic simulations.

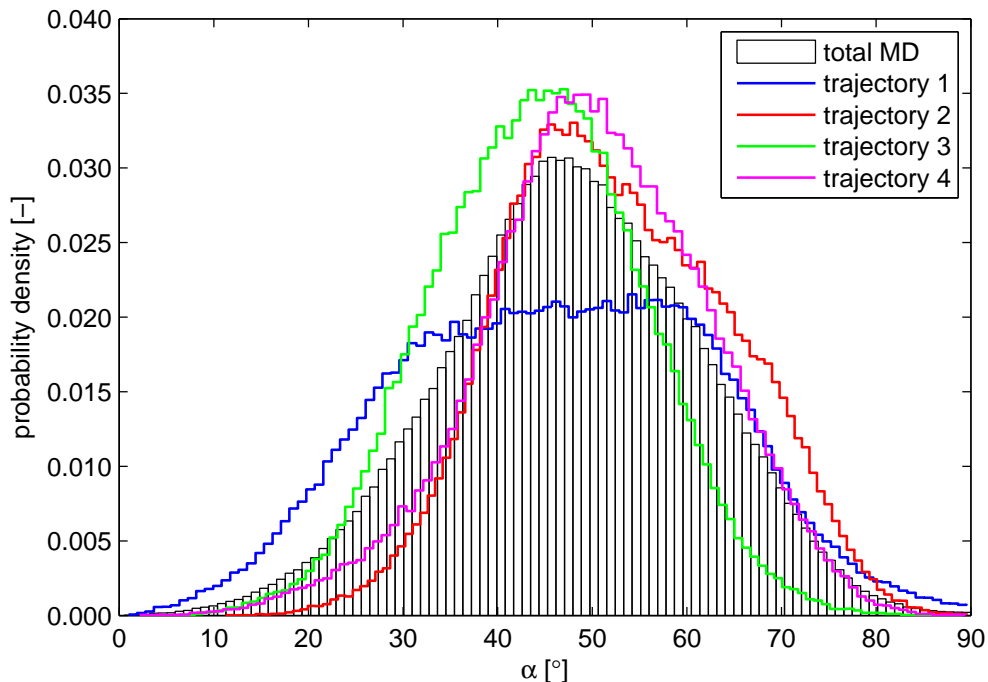


Figure 5.6: Orientational distributions from individual MD trajectories compared to the overall orientational distribution from MD.

The slow convergence of the simulation results reflects the rather slow dynamics and high complexity of the membrane environment. This becomes even more pronounced if one tries to simulate molecules in membranes stiffened by high amounts of cholesterol. Our preliminary results on the F2N12S probe in a membrane containing 40 mol % of cholesterol reveal problematic convergence of conventional MD at relevant temperatures because of high energetic barriers hindering changes in the probe’s location and orientation. To overcome these difficulties, we have just begun work on an alternative method to acquire the orientational distribution, relying on the potential of mean force calculated using umbrella sampling (Roux, 1995).

trajectory	mean [°]	standard deviation [°]
1	46	16
2	52	12
3	44	11
4	50	12
average	48 ± 4	13 ± 2

Table 5.2: Means and standard deviations of orientational distributions obtained from individual MD trajectories and their average values with the 95% confidence intervals.

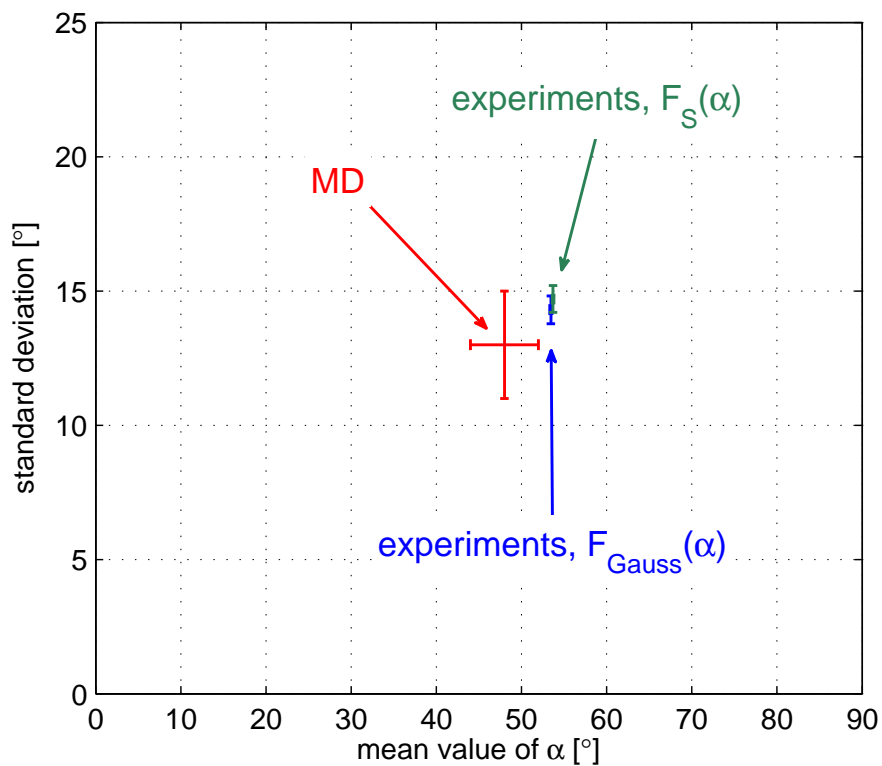


Figure 5.7: Comparison of mean values and standard deviations of orientational distributions obtained from MD trajectories and from experiments. $F_{Gauss}(\alpha)$ denotes the Gaussian-based estimate and $F_S(\alpha)$ the entropy-maximizing distribution. The error bars indicate the 95% confidence intervals.

Conclusion

The goal of this thesis was to investigate whether linear dichroism measurements can serve as a reliable method for obtaining accurate information on orientational distributions of fluorescent probes in lipid membranes, and whether molecular dynamics simulations together with quantum calculations of one-photon and two-photon absorption properties can offer a solid basis for the interpretation of experimental data. In order to directly compare simulations with experiments, we chose to examine a model system formed by a POPC bilayer containing the F2N12S probe.

Experimentally, the model system was realized using F2N12S-labeled giant unilamellar vesicles. We measured one-photon and two-photon linear dichroism of the F2N12S probe embedded in the vesicles and used several approaches to reconstruct the orientational distribution of the one-photon transition dipole moment of the F2N12S probe relative to the membrane normal. All the approaches revealed a broad distribution of orientations with a single peak positioned around a tilt angle of 50° – 55° relative to the membrane normal.

At the same time, we performed molecular dynamics simulations of an F2N12S probe in a POPC bilayer. Despite starting with the probe placed outside the bilayer, we observed a relatively fast spontaneous stabilization of the probe within the bilayer. We analyzed the location of the probe in the membrane as well as its contacts with the surrounding molecules and related these findings to already published experimental data. Next, we performed one-photon transition dipole moment calculations for a series of geometries extracted from the trajectories, with the environment being modeled as point charges, and we characterized the direction of the one-photon transition dipole moment relative to the molecular geometry. Subsequently, we discussed conditions leading to a substantial simplification of the description of two-photon absorption anisotropy and performed calculations indicating that these conditions were satisfied by the F2N12S probe. Finally, we combined the results of molecular dynamics and quantum calculations to determine the orientational distribution from simulations. Analyzing separately orientational distributions gained from four independent trajectories, we pointed out the need for a long sampling time to achieve full convergence. Although not reaching perfectly converged orientational distributions for the independent trajectories, the overall results of molecular dynamics yielded enough information to allow for a quantitative comparison with experiments.

The comparison of the overall orientational distribution acquired from molecular dynamics with the experimental results revealed a good agreement between

the simulations and experiments, with the mean values of the distributions being shifted by less than 6° and the standard deviations differing by less than 2° . Moreover, we found that the orientational distribution obtained from molecular dynamics had a Gaussian shape, verifying, at least for the present system and possibly also for a broader category of fluorescent probes embedded in lipid membranes in the liquid disordered phase, one of the present approaches to reconstruct the orientational distribution from experiments. We report on these findings in (Timr et al., submitted).

The good agreement between simulations and experiments shows that the combination of one-photon and two-photon linear dichroism measurements can be used to gain insight into molecular orientations. Further work is needed to extend the current results to membranes with more complex lipid compositions and to larger fluorescent molecules, including fluorescently labeled membrane proteins. Assisted by simulations, linear dichroism measurements have a potential to become a powerful tool to study structures and processes in living cells.

Bibliography

- B. Alberts, A. Johnson, J. Lewis, M. Raff, K. Roberts, and P. Walter. *Molecular Biology of the Cell*. Garland Science, New York, 4th edition, 2002.
- M. P. Allen and D. J. Tildesley. *Computer Simulation of Liquids*. Oxford science publications. Clarendon Press; Oxford University Press, Oxford, 1989.
- H. C. Andersen. Molecular dynamics simulations at constant pressure and/or temperature. *Journal of Chemical Physics*, 72(4):2384–2393, 1980.
- C. Angeli, K. L. Bak, V. Bakken, O. Christiansen, R. C. S. Coriani, P. Dahle, E. K. Dalskov, T. Enevoldsen, B. Fernandez, C. Hättig, K. Hald, A. Halkier, H. Heiberg, T. Helgaker, H. Hettema, H. J. A. Jensen, D. Jonsson, P. Jorgensen, S. Kirpekar, W. Klopper, R. Kobayashi, H. Koch, A. Ligabue, O. B. Lutnaes, K. V. Mikkelsen, P. Norman, J. Olsen, M. J. Packer, T. B. Pedersen, Z. Rinkevicius, E. Rudberg, T. A. Ruden, K. Ruud, P. Salek, A. S. de Meras, T. Saue, S. P. A. Sauer, B. Schimmelpfennig, K. O. Sylvester-Hvid, P. R. Taylor, O. Vahtras, D. J. Wilson, , and H. Agren. DALTON, a molecular electronic structure program, release dalton2011, 2011. URL <http://daltonprogram.org>.
- M. I. Angelova and D. S. Dimitrov. Liposome electroformation. *Faraday Discussions*, 81:303–311, 1986.
- A. D. Becke. Density-functional thermochemistry. III. The role of exact exchange. *Journal of Chemical Physics*, 98(7):5648–5652, 1993.
- R. K. P. Benninger, B. Onfelt, M. A. A. Neil, D. M. Davis, and P. M. W. French. Fluorescence imaging of two-photon linear dichroism: cholesterol depletion disrupts molecular orientation in cell membranes. *Biophysical Journal*, 88(1):609–622, 2005.
- H. J. C. Berendsen, J. P. M. Postma, W. F. van Gunsteren, and J. Hermans. *Interaction Models for Water in Relation to Protein Hydration*, pages 331–342. D. Reidel Publishing Company, Dordrecht, 1981.
- H. J. C. Berendsen, J. P. M. Postma, W. F. van Gunsteren, A. Dinola, and J. R. Haak. Molecular dynamics with coupling to an external bath. *Journal of Chemical Physics*, 81(8):3684–3690, 1984.
- O. Berger, O. Edholm, and F. Jahnig. Molecular dynamics simulations of a fluid bilayer of dipalmitoylphosphatidylcholine at full hydration, constant pressure, and constant temperature. *Biophysical Journal*, 72(5):2002–2013, 1997.

- R. W. Boyd. *Nonlinear Optics*. Academic Press, Amsterdam, 3rd edition, 2008.
- J. J. L. Cascales, M. L. Huertas, and J. G. de la Torre. Molecular dynamics simulation of a dye molecule in the interior of a bilayer: 1,6-diphenyl-1,3,5-hexatriene in dipalmitoylphosphatidylcholine. *Biophysical Chemistry*, 69(1):1–8, 1997.
- M. Castanho, S. Lopes, and M. Fernandes. Using UV-Vis. linear dichroism to study the orientation of molecular probes and biomolecules in lipidic membranes. *Spectroscopy*, 17(2-3):377–398, 2003.
- D. Chandler. *Introduction to Modern Statistical Mechanics*. Oxford University Press, New York, 1987.
- I. Chandrasekhar, M. Kastenzholz, R. D. Lins, C. Oostenbrink, L. D. Schuler, D. P. Tieleman, and W. F. van Gunsteren. A consistent potential energy parameter set for lipids: dipalmitoylphosphatidylcholine as a benchmark of the GROMOS96 45A3 force field. *European Biophysics Journal with Biophysics Letters*, 32(1):67–77, 2003.
- S. W. Chiu, M. Clark, V. Balaji, S. Subramaniam, H. L. Scott, and E. Jakobsson. Incorporation of surface tension into molecular dynamics simulation of an interface: a fluid phase lipid bilayer membrane. *Biophysical Journal*, 69(4):1230–1245, 1995.
- D. P. Craig and T. Thirunamachandran. *Molecular Quantum Electrodynamics: An Introduction to Radiation-Molecule Interactions*. Academic Press, London, 1st edition, 1984.
- C. J. Cramer. *Essentials of Computational Chemistry: Theories and Models*. John Wiley, Chichester, 1st edition, 2002.
- L. Cwiklik, A. J. A. Aquino, M. Vazdar, P. Jurkiewicz, J. Pittner, M. Hof, and H. Lischka. Absorption and fluorescence of PRODAN in phospholipid bilayers: a combined quantum mechanics and classical molecular dynamics study. *Journal of Physical Chemistry A*, 115(41):11428–11437, 2011.
- T. Darden, D. York, and L. Pedersen. Particle mesh Ewald: an $N \cdot \log(N)$ method for Ewald sums in large systems. *Journal of Chemical Physics*, 98(12):10089–10092, 1993.
- A. Darszon, C. A. Vandenberg, M. Schonfeld, M. H. Ellisman, N. C. Spitzer, and M. Montal. Reassembly of protein-lipid complexes into large bilayer vesicles: perspectives for membrane reconstitution. *Proceedings of the National Academy*

- of Sciences of the United States of America-Biological Sciences*, 77(1):239–243, 1980.
- R. Das, A. S. Klymchenko, G. Duportail, and Y. Mély. Excited state proton transfer and solvent relaxation of a 3-hydroxyflavone probe in lipid bilayers. *Journal of Physical Chemistry B*, 112(38):11929–11935, 2008.
- F. de Chaumont, S. Dallongeville, N. Chenouard, N. Herve, S. Pop, T. Provoost, V. Meas-Yedid, P. Pankajakshan, T. Lecomte, Y. Le Montagner, T. Lagache, A. Dufour, and J. C. Olivo-Marin. Icy: an open bioimage informatics platform for extended reproducible research. *Nature Methods*, 9(7):690–696, 2012.
- R. Delgado-Gonzalo, P. Thevenaz, C. S. Seelamantula, and M. Unser. Snakes with an ellipse-reproducing property. *IEEE Transactions on Image Processing*, 21(3):1258–1271, 2012a.
- R. Delgado-Gonzalo, P. Thevenaz, and M. Unser. Exponential splines and minimal-support bases for curve representation. *Computer Aided Geometric Design*, 29(2):109–128, 2012b.
- A. P. Demchenko, Y. Mély, G. Duportail, and A. S. Klymchenko. Monitoring biophysical properties of lipid membranes by environment-sensitive fluorescent probes. *Biophysical Journal*, 96(9):3461–3470, 2009.
- A. Dreuw and M. Head-Gordon. Single-reference ab initio methods for the calculation of excited states of large molecules. *Chemical Reviews*, 105(11):4009–4037, 2005.
- M. Drobizhev, F. Q. Meng, A. Rebane, Y. Stepanenko, E. Nickel, and C. W. Spangler. Strong two-photon absorption in new asymmetrically substituted porphyrins: interference between charge-transfer and intermediate-resonance pathways. *Journal of Physical Chemistry B*, 110(20):9802–9814, 2006.
- T. H. Dunning. Gaussian basis sets for use in correlated molecular calculations. I. The atoms boron through neon and hydrogen. *Journal of Chemical Physics*, 90(2):1007–1023, 1989.
- U. Essmann, L. Perera, M. L. Berkowitz, T. Darden, H. Lee, and L. G. Pedersen. A smooth particle mesh Ewald method. *Journal of Chemical Physics*, 103(19):8577–8593, 1995.
- P. P. Ewald. Die Berechnung optischer und elektrostatischer Gitterpotentiale. *Annalen der Physik*, 64:253–287, 1921.

- E. R. Farkas and W. W. Webb. Multiphoton polarization imaging of steady-state molecular order in ternary lipid vesicles for the purpose of lipid phase assignment. *Journal of Physical Chemistry B*, 114(47):15512–15522, 2010.
- S. E. Feller and A. D. MacKerell. An improved empirical potential energy function for molecular simulations of phospholipids. *Journal of Physical Chemistry B*, 104(31):7510–7515, 2000.
- M. Fraňová, J. Repáková, P. Čapková, J. M. Holopainen, and I. Vattulainen. Effects of DPH on DPPC-cholesterol membranes with varying concentrations of cholesterol: from local perturbations to limitations in fluorescence anisotropy experiments. *Journal of Physical Chemistry B*, 114(8):2704–2711, 2010.
- L. Frediani, Z. Rinkevicius, and H. Agren. Two-photon absorption in solution by means of time-dependent density-functional theory and the polarizable continuum model. *Journal of Chemical Physics*, 122(24), 2005.
- M. J. Frisch, G. W. Trucks, H. B. Schlegel, G. E. Scuseria, M. A. Robb, J. R. Cheeseman, G. Scalmani, V. Barone, B. Mennucci, G. A. Petersson, H. Nakatsuji, M. Caricato, X. Li, H. P. Hratchian, A. F. Izmaylov, J. Bloino, G. Zheng, J. L. Sonnenberg, M. Hada, M. Ehara, K. Toyota, R. Fukuda, J. Hasegawa, M. Ishida, T. Nakajima, Y. Honda, O. Kitao, H. Nakai, T. Vreven, J. A. Montgomery, Jr., J. E. Peralta, F. Ogliaro, M. Bearpark, J. J. Heyd, E. Brothers, K. N. Kudin, V. N. Staroverov, R. Kobayashi, J. Normand, K. Raghavachari, A. Rendell, J. C. Burant, S. S. Iyengar, J. Tomasi, M. Cossi, N. Rega, J. M. Millam, M. Klene, J. E. Knox, J. B. Cross, V. Bakken, C. Adamo, J. Jaramillo, R. Gomperts, R. E. Stratmann, O. Yazyev, A. J. Austin, R. Cammi, C. Pomelli, J. W. Ochterski, R. L. Martin, K. Morokuma, V. G. Zakrzewski, G. A. Voth, P. Salvador, J. J. Dannenberg, S. Dapprich, A. D. Daniels, . Farkas, J. B. Foresman, J. V. Ortiz, J. Cioslowski, and D. J. Fox. Gaussian 09, revision a.02, 2009.
- R. R. Gullapalli, M. C. Demirel, and P. J. Butler. Molecular dynamics simulations of DiI-C-18(3) in a DPPC lipid bilayer. *Physical Chemistry Chemical Physics*, 10(24):3548–3560, 2008.
- J. Hermans, H. J. C. Berendsen, W. F. van Gunsteren, and J. P. M. Postma. A consistent empirical potential for water-protein interactions. *Biopolymers*, 23(8):1513–1518, 1984.
- B. Hess, H. Bekker, H. J. C. Berendsen, and J. Fraaije. LINCS: a linear constraint solver for molecular simulations. *Journal of Computational Chemistry*, 18(12):1463–1472, 1997.

- M. J. Hinner, S. J. Marrink, and A. H. de Vries. Location, tilt, and binding: a molecular dynamics study of voltage-sensitive dyes in biomembranes. *Journal of Physical Chemistry B*, 113(48):15807–15819, 2009.
- R. W. Hockney, S. P. Goel, and J. W. Eastwood. Quiet high-resolution computer models of a plasma. *Journal of Computational Physics*, 14(2):148–158, 1974.
- M. Hof, R. Hutterer, and V. Fidler. *Fluorescence Spectroscopy in Biology: Advanced Methods and their Applications to Membranes, Proteins, DNA, and Cells*. Springer series on fluorescence. Springer, Berlin, 2005.
- B. Hoff, E. Strandberg, A. S. Ulrich, D. P. Tieleman, and C. Posten. 2H-NMR study and molecular dynamics simulation of the location, alignment, and mobility of pyrene in POPC bilayers. *Biophysical Journal*, 88(3):1818–1827, 2005.
- M. Holtta-Vuori, R. L. Uronen, J. Repáková, E. Salonen, I. Vattulainen, P. Panula, Z. G. Li, R. Bittman, and E. Ikonen. BODIPY-cholesterol: a new tool to visualize sterol trafficking in living cells and organisms. *Traffic*, 9(11):1839–1849, 2008.
- W. G. Hoover. Canonical dynamics: equilibrium phase-space distributions. *Physical Review A*, 31(3):1695–1697, 1985.
- B. Jojart and T. A. Martinek. Performance of the general amber force field in modeling aqueous POPC membrane bilayers. *Journal of Computational Chemistry*, 28(12):2051–2058, 2007.
- W. L. Jorgensen and J. Tirado-Rives. The OPLS potential functions for proteins. Energy minimizations for crystals of cyclic-peptides and crambin. *Journal of the American Chemical Society*, 110(6):1657–1666, 1988.
- A. Karotki. Simultaneous two-photon absorption of tetrapyrrolic molecules: from femtosecond coherence experiments to photodynamic therapy. Ph.D. thesis, Montana State University, Bozeman, Montana, 2003. URL etd.lib.montana.edu/etd/2003/karotki/KarotkiA03.pdf.
- A. S. Klymchenko, G. Duportail, A. P. Demchenko, and Y. Mély. Bimodal distribution and fluorescence response of environment-sensitive probes in lipid bilayers. *Biophysical Journal*, 86(5):2929–2941, 2004a.
- A. S. Klymchenko, Y. Mély, A. P. Demchenko, and G. Duportail. Simultaneous probing of hydration and polarity of lipid bilayers with 3-hydroxyflavone fluorescent dyes. *Biochimica Et Biophysica Acta-Biomembranes*, 1665(1-2):6–19, 2004b.

- A. S. Klymchenko, S. Oncul, P. Didier, E. Schaub, L. Bagatolli, G. Duportail, and Y. Mély. Visualization of lipid domains in giant unilamellar vesicles using an environment-sensitive membrane probe based on 3-hydroxyflavone. *Biochimica Et Biophysica Acta-Biomembranes*, 1788(2):495–499, 2009.
- A. Kyrychenko. A molecular dynamics model of rhodamine-labeled phospholipid incorporated into a lipid bilayer. *Chemical Physics Letters*, 485(1-3):95–99, 2010.
- J. R. Lakowicz. *Principles of Fluorescence Spectroscopy*. Springer, New York, 3rd edition, 2006.
- J. Lazar, A. Bondar, S. Timr, and S. J. Firestein. Two-photon polarization microscopy reveals protein structure and function. *Nature Methods*, 8(8):684–690, 2011.
- Life Technologies. Product spectra - F2N12S/lipid, accessed April 2, 2013. URL <http://www.invitrogen.com/site/us/en/home/support/Product-Technical-Resources/Product-Spectra.F2N12S.html>.
- D. Lingwood and K. Simons. Lipid rafts as a membrane-organizing principle. *Science*, 327(5961):46–50, 2010.
- L. M. S. Loura and J. P. P. Ramalho. Location and dynamics of acyl chain NBD-labeled phosphatidylcholine (NBD-PC) in DPPC bilayers. A molecular dynamics and time-resolved fluorescence anisotropy study. *Biochimica Et Biophysica Acta-Biomembranes*, 1768(3):467–478, 2007.
- L. M. S. Loura and J. P. P. Ramalho. Recent developments in molecular dynamics simulations of fluorescent membrane probes. *Molecules*, 16(7):5437–5452, 2011.
- L. M. S. Loura, F. Fernandes, A. C. Fernandes, and J. P. P. Ramalho. Effects of fluorescent probe NBD-PC on the structure, dynamics and phase transition of DPPC. A molecular dynamics and differential scanning calorimetry study. *Biochimica Et Biophysica Acta-Biomembranes*, 1778(2):491–501, 2008.
- L. M. S. Loura, A. J. P. Carvalho, and J. P. P. Ramalho. Direct calculation of Förster orientation factor of membrane probes by molecular simulation. *Journal of Molecular Structure-Theochem*, 946(1-3):107–112, 2010.
- L. M. S. Loura, P. Carvalho, and J. P. P. Ramalho. Recent developments in the study of the behavior of fluorescent membrane probes in lipid bilayers: molecular dynamics approach. In A. N. Misra, editor, *Biophysics*. InTech, 2012. doi: 10.5772/35468.

- A. P. Lyubartsev and A. L. Rabinovich. Recent development in computer simulations of lipid bilayers. *Soft Matter*, 7(1):25–39, 2011.
- A. D. MacKerell, J. Wiorkiewicz-Kuczera, and M. Karplus. An all-atom empirical energy function for the simulation of nucleic acids. *Journal of the American Chemical Society*, 117(48):11946–11975, 1995.
- A. D. MacKerell, D. Bashford, M. Bellott, R. L. Dunbrack, J. D. Evanseck, M. J. Field, S. Fischer, J. Gao, H. Guo, S. Ha, D. Joseph-McCarthy, L. Kuchnir, K. Kuczera, F. T. K. Lau, C. Mattos, S. Michnick, T. Ngo, D. T. Nguyen, B. Prodhom, W. E. Reiher, B. Roux, M. Schlenkrich, J. C. Smith, R. Stote, J. Straub, M. Watanabe, J. Wiorkiewicz-Kuczera, D. Yin, and M. Karplus. All-atom empirical potential for molecular modeling and dynamics studies of proteins. *Journal of Physical Chemistry B*, 102(18):3586–3616, 1998.
- A. E. Mark, S. P. van Helden, P. E. Smith, L. H. M. Janssen, and W. F. van Gunsteren. Convergence properties of free energy calculations: alpha-cyclodextrin complexes as a case study. *Journal of American Chemical Society*, 116(14):6293–6302, 1994.
- M. A. L. Marques, N. T. Maitra, F. Nogueira, E. K. U. Gross, and A. Rubio. *Fundamentals of Time-Dependent Density Functional Theory*. Springer-Verlag, Heidelberg, 2012.
- S. J. Marrink, H. J. Risselada, S. Yefimov, D. P. Tieleman, and A. H. de Vries. The MARTINI force field: coarse grained model for biomolecular simulations. *Journal of Physical Chemistry B*, 111(27):7812–7824, 2007.
- L. Mathivet, S. Cribier, and P. F. Devaux. Shape change and physical properties of giant phospholipid vesicles prepared in the presence of an AC electric field. *Biophysical Journal*, 70(3):1112–1121, 1996.
- S. Miyamoto and P. A. Kollman. SETTLE: an analytical version of the SHAKE and RATTLE algorithm for rigid water models. *Journal of Computational Chemistry*, 13(8):952–962, 1992.
- N. F. Morales-Pennington, J. Wu, E. R. Farkas, S. L. Goh, T. M. Konyakhina, J. Y. Zheng, W. W. Webb, and G. W. Feigenson. GUV preparation and imaging: minimizing artifacts. *Biochimica Et Biophysica Acta-Biomembranes*, 1798(7):1324–1332, 2010.
- H. S. Muddana, R. R. Gullapalli, E. Manias, and P. J. Butler. Atomistic simulation of lipid and DiI dynamics in membrane bilayers under tension. *Physical Chemistry Chemical Physics*, 13(4):1368–1378, 2011.

- D. Needham, T. J. McIntosh, and E. Evans. Thermomechanical and transition properties of dimyristoylphosphatidylcholine cholesterol bilayers. *Biochemistry*, 27(13):4668–4673, 1988.
- S. Nosé and M. L. Klein. Constant pressure molecular dynamics for molecular systems. *Molecular Physics*, 50(5):1055–1076, 1983.
- N. M. O’Boyle, M. Banck, C. A. James, C. Morley, T. Vandermeersch, and G. R. Hutchison. Open Babel: an open chemical toolbox. *Journal of Cheminformatics*, 3, 2011. doi: 10.1186/1758-2946-3-33.
- J. Olsen and P. Jorgensen. Linear and nonlinear response functions for an exact state and for an MCSCF state. *Journal of Chemical Physics*, 82(7):3235–3264, 1985.
- S. Oncul, A. S. Klymchenko, O. A. Kucherak, A. P. Demchenko, S. Martin, M. Dontenwill, Y. Arntz, P. Didier, G. Duportail, and Y. Mély. Liquid ordered phase in cell membranes evidenced by a hydration-sensitive probe: effects of cholesterol depletion and apoptosis. *Biochimica Et Biophysica Acta-Biomembranes*, 1798(7):1436–1443, 2010.
- M. Parrinello and A. Rahman. Polymorphic transitions in single-crystals: a new molecular dynamics method. *Journal of Applied Physics*, 52(12):7182–7190, 1981.
- D. W. Piston. Imaging living cells and tissues by two-photon excitation microscopy. *Trends in Cell Biology*, 9(2):66–69, 1999.
- M. Reed and B. Simon. *Methods of Modern Mathematical Physics III: Scattering Theory*, pages 149–151. Academic Press, San Diego, 1st edition, 1979.
- J. E. Reeve, A. D. Corbett, I. Boczarow, T. Wilson, H. Bayley, and H. L. Anderson. Probing the orientational distribution of dyes in membranes through multiphoton microscopy. *Biophysical Journal*, 103(5):907–917, 2012.
- J. P. Reeves and R. M. Dowben. Formation and properties of thin-walled phospholipid vesicles. *Journal of Cellular Physiology*, 73(1):49–60, 1969.
- J. Repáková, P. Čapková, J. M. Holopainen, and I. Vattulainen. Distribution, orientation, and dynamics of DPH probes in DPPC bilayer. *Journal of Physical Chemistry B*, 108(35):13438–13448, 2004.
- J. Repáková, J. M. Holopainen, M. R. Morrow, M. C. McDonald, P. Čapková, and I. Vattulainen. Influence of DPH on the structure and dynamics of a DPPC bilayer. *Biophysical Journal*, 88(5):3398–3410, 2005.

- J. Repáková, J. M. Holopainen, M. Karttunen, and I. Vattulainen. Influence of pyrene-labeling on fluid lipid membranes. *Journal of Physical Chemistry B*, 110(31):15403–15410, 2006.
- N. Rodriguez, F. Pincet, and S. Cribier. Giant vesicles formed by gentle hydration and electroformation: a comparison by fluorescence microscopy. *Colloids and Surfaces B-Biointerfaces*, 42(2):125–130, 2005.
- B. Roux. The calculation of the potential of mean force using computer simulations. *Computer Physics Communications*, 91(1-3):275–282, 1995.
- P. Salek, O. Vahtras, T. Helgaker, and H. Agren. Density-functional theory of linear and nonlinear time-dependent molecular properties. *Journal of Chemical Physics*, 117(21):9630–9645, 2002.
- P. Salek, O. Vahtras, J. D. Guo, Y. Luo, T. Helgaker, and H. Agren. Calculations of two-photon absorption cross sections by means of density-functional theory. *Chemical Physics Letters*, 374(5-6):446–452, 2003.
- A. Schafer, H. Horn, and R. Ahlrichs. Fully optimized contracted Gaussian basis sets for atoms Li to Kr. *Journal of Chemical Physics*, 97(4):2571–2577, 1992.
- L. D. Schuler, X. Daura, and W. F. van Gunsteren. An improved GROMOS96 force field for aliphatic hydrocarbons in the condensed phase. *Journal of Computational Chemistry*, 22(11):1205–1218, 2001.
- A. W. Schuttelkopf and D. M. F. van Aalten. PRODRG: a tool for high-throughput crystallography of protein-ligand complexes. *Acta Crystallographica Section D-Biological Crystallography*, 60:1355–1363, 2004.
- V. V. Shynkar, A. S. Klymchenko, C. Kunzelmann, G. Duportail, C. D. Muller, A. P. Demchenko, J. M. Freyssinet, and Y. Mély. Fluorescent biomembrane probe for ratiometric detection of apoptosis. *Journal of the American Chemical Society*, 129(7):2187–2193, 2007.
- K. Simons and E. Ikonen. Functional rafts in cell membranes. *Nature*, 387(6633):569–572, 1997.
- S. J. Singer and G. L. Nicolson. Fluid mosaic model of structure of cell-membranes. *Science*, 175(4023):720–731, 1972.
- U. C. Singh and P. A. Kollman. An approach to computing electrostatic charges for molecules. *Journal of Computational Chemistry*, 5(2):129–145, 1984.

- M. J. Skaug, M. L. Longo, and R. Faller. Computational studies of Texas Red-1,2-dihexadecanoyl-sn-glycero-3-phosphoethanolamine - model building and applications. *Journal of Physical Chemistry B*, 113(25):8758–8766, 2009.
- K. C. Song, P. W. Livanec, J. B. Klauda, K. Kuczera, R. C. Dunn, and W. Im. Orientation of fluorescent lipid analogue BODIPY-PC to probe lipid membrane properties: insights from molecular dynamics simulations. *Journal of Physical Chemistry B*, 115(19):6157–6165, 2011.
- M. Stöckl, J. Nikolaus, and A. Herrmann. Visualization of lipid domain-specific protein sorting in giant unilamellar vesicles. *Liposomes: Methods and Protocols, Vol 2: Biological Membrane Models*, 606:115–126, 2010.
- M. T. Stöckl and A. Herrmann. Detection of lipid domains in model and cell membranes by fluorescence lifetime imaging microscopy. *Biochimica Et Biophysica Acta-Biomembranes*, 1798(7):1444–1456, 2010.
- K. Svoboda and R. Yasuda. Principles of two-photon excitation microscopy and its applications to neuroscience. *Neuron*, 50(6):823–839, 2006.
- W. C. Swope, H. C. Andersen, P. H. Berens, and K. R. Wilson. A computer simulation method for the calculation of equilibrium-constants for the formation of physical clusters of molecules: application to small water clusters. *Journal of Chemical Physics*, 76(1):637–649, 1982.
- S. Timr, A. Bondar, L. Cwiklik, M. Štefl, M. Vazdar, J. Lazar, and P. Jungwirth. Accurate determination of orientational distribution of a fluorescent dye in a model membrane by linear dichroism measurements and molecular simulations. *Journal of Physical Chemistry B*, submitted.
- A. R. van Buuren, S. J. Marrink, and H. J. C. Berendsen. A molecular dynamics study of the decane water interface. *Journal of Physical Chemistry*, 97(36):9206–9212, 1993.
- D. van der Spoel, E. Lindahl, B. Hess, A. R. van Buuren, E. Apol, P. J. Meulenhoff, D. P. Tieleman, A. L. T. M. Sijbers, K. A. Feenstra, R. van Drunen, and H. J. C. Berendsen. Gromacs user manual version 4.5.2, 2010. URL www.gromacs.org.
- W. F. van Gunsteren and H. J. C. Berendsen. *GROMOS-87 Manual*. Biomos BV, Nijenborgh 4, 9747 AG Groningen, The Netherlands, 1987.

- J. Čurdová, P. Čapková, J. Plášek, J. Repáková, and I. Vattulainen. Free pyrene probes in gel and fluid membranes: perspective through atomistic simulations. *Journal of Physical Chemistry B*, 111(14):3640–3650, 2007.
- L. Verlet. Computer experiments on classical fluids. I. Thermodynamical properties of Lennard-Jones molecules. *Physical Review*, 159(1):98–103, 1967.
- J. M. Wang, R. M. Wolf, J. W. Caldwell, P. A. Kollman, and D. A. Case. Development and testing of a general Amber force field. *Journal of Computational Chemistry*, 25(9):1157–1174, 2004.
- T. Yanai, D. P. Tew, and N. C. Handy. A new hybrid exchange-correlation functional using the Coulomb-attenuating method (CAM-B3LYP). *Chemical Physics Letters*, 393(1-3):51–57, 2004.

List of Tables

1.1	Orientational distribution parameters with their 95 % confidence intervals obtained by fitting a combination of 1P and 2P experimental data on the F2N12S probe in POPC GUVs.	20
2.1	Atom types of the GROMOS-87 and Berger lipids force fields, atomic charges, and charge groups used to parametrize the F2N12S probe.	32
2.2	Values of dihedral parameters obtained from quantum scans.	33
3.1	Comparison of the 1P TDM directions yielded by B3LYP and CAM-B3LYP for a B3LYP/cc-pVDZ optimized geometry in vacuum.	49
3.2	Dependence of the 1P TDM direction on the choice of basis set for a B3LYP/cc-pVDZ optimized geometry in vacuum.	50
4.1	Eigenvalues of the 2P transition tensor between states S_0 and S_1 of the F2N12S probe.	55
5.1	Comparison of means and standard deviations of orientational distributions obtained from MD simulations and experiments.	59
5.2	Means and standard deviations of orientational distributions obtained from individual MD trajectories and their average values with the 95% confidence intervals.	62

List of Abbreviations

1P	one-photon
1P TDM	one-photon transition dipole moment
2P	two-photon
AFM	atomic-force microscopy
DFT	density functional theory
EPR	electron paramagnetic resonance
FA	fluorescence anisotropy
GUV	giant unilamellar vesicle
LD	linear dichroism
LUV	large unilamellar vesicle
MD	molecular dynamics
NMR	nuclear magnetic resonance
PBC	periodic boundary conditions
SUV	small unilamellar vesicle
TD-DFT	time-dependent density functional theory